ACS APPLIED MATERIALS & INTERFACES

www.acsami.org Research Article

Mechanisms of Hysteresis and Reversibility across the Voltage-Driven Perovskite–Brownmillerite Transformation in Electrolyte-Gated Ultrathin $La_{0.5}Sr_{0.5}CoO_{3-\delta}$

William M. Postiglione, Guichuan Yu, Vipul Chaturvedi, Hua Zhou, Kei Heltemes, Andrew Jacobson, Martin Greven, and Chris Leighton*

Cite This: *ACS Appl. Mater. Interfaces* 2024, 16, 19184–19197

Read Online

ACCESS | Metrics & More | Article Recommendations | Supporting Information

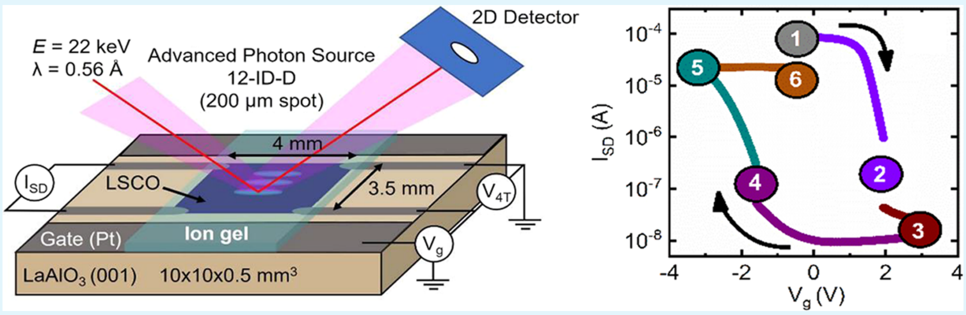

ABSTRACT: Perovskite cobaltites have emerged as archetypes for electrochemical control of materials properties in electrolyte-gate devices. Voltage-driven redox cycling can be performed between fully oxygenated perovskite and oxygen-vacancy-ordered brownmillerite phases, enabling exceptional modulation of the crystal structure, electronic transport, thermal transport, magnetism, and optical properties. The vast majority of studies, however, have focused heavily on the perovskite and brownmillerite end points. In contrast, here we focus on hysteresis and reversibility across the entire perovskite ↔ brownmillerite topotactic transformation, combining gate-voltage hysteresis loops, minor hysteresis loops, quantitative operando synchrotron X-ray diffraction, and temperature-dependent (magneto)transport, on ion-gel-gated ultrathin (10-unit-cell) epitaxial $La_{0.5}Sr_{0.5}CoO_{3-\delta}$ films. Gate-voltage hysteresis loops combined with operando diffraction reveal a wealth of new mechanistic findings, including asymmetric redox kinetics due to differing oxygen diffusivities in the two phases, nonmonotonic transformation rates due to the first-order nature of the transformation, and limits on reversibility due to first-cycle structural degradation. Minor loops additionally enable the first rational design of an optimal gate-voltage cycle. Combining this knowledge, we demonstrate state-of-the-art nonvolatile cycling of electronic and magnetic properties, encompassing $>10^5$ transport ON/OFF ratios at room temperature, and reversible metal–insulator–metal and ferromagnet–nonferromagnet–ferromagnet cycling, all at 10-unit-cell thickness with high room-temperature stability. This paves the way for future work to establish the ultimate cycling frequency and endurance of such devices.

KEYWORDS: *electrolyte gating, magnetoionics, complex oxides, perovskite–brownmillerite transformation, hysteresis, reversibility*

■ INTRODUCTION

Recent years have seen dramatic expansion of interest in the area of electric-field or voltage control of materials properties via electrochemical mechanisms. It is now understood that this can be achieved via ionic liquids and gels,[1−5] solid electrolytes,[2,5−7] and ionic conductors,[2,5−7] utilizing these media to control the insertion/extraction of various chemical species into/out of target materials they are interfaced with. These species include oxygen ions/vacancies (O/V_O),[2−33] H ions,[2,5−7,13,25,28,30,31,34,35] Li ions,[28,36,37] N ions,[38,39] F ions,[40] etc., inserted/extracted into/from a variety of target materials, spanning metals,[5−7,9,10,35,37] oxides,[2−8,11−34,40] two-dimensional materials,[3−5,28,36] nitrides,[38,39] polymer semiconductors,[1,3] and more. Devices operating on these principles are electrochemical transistors, where a gate voltage (V_g) across the electrolyte or ionic conductor controls the properties of the target material electrode through ion insertion/extraction, merging concepts from materials science, electrochemistry, physics, and electrical engineering. The resulting modulation of materials properties spans extraordinary ranges of electronic,[1−5,8,11−30,34,36,37] magnetic,[2−7,9,10,13−22,31−33,35,37−39]

Received: January 23, 2024
Revised: March 12, 2024
Accepted: March 15, 2024
Published: April 2, 2024

thermal,[3,23,25] and optical[3,13,16−18,29−31] properties, leading to device potential in magnetoionics,[2−7,9,10,13−22,31−33,35,37−39] neuromorphic and stochastic computing,[2,5−7,41] thermal management,[3,23,25,28] voltage-tuned photonics,[2,3,28,29] etc. In addition to exceptional property modulation, this approach also offers nonvolatility, low power consumption, reversibility, and competitive frequencies for many applications, although the ultimate limits on frequency and endurance remain unclear.[2]

Complex oxides have emerged as premier examples of the power of this approach,[2−5,11−33] particularly perovskite cobaltites such as $SrCoO_{3-\delta}$.[11−14,16,19−21,24−27,31] These materials offer low free energies of formation of V_O (ΔG_{V_o}),[4,42−45] high diffusivities of V_O (D_{V_o}), even at ambient temperature,[4,46−48] and very different properties in fully oxygenated and reduced states,[49,50] ideal attributes for V_g-actuated redox-based electrochemical control. As the V_O concentration is increased, this system in fact topotactically transforms from cubic perovskite (P) $SrCoO_{3-\delta}$ with disordered V_O to orthorhombic brownmillerite (BM) $SrCoO_{2.5}$ ($Sr_2Co_2O_5$) with ordered V_O.[51,52] These structures are illustrated in Figure 1(a), where the BM exhibits alternating O-sufficient and O-deficient planes, with octahedral and tetrahedral Co−O coordination, respectively.[50,53,54] The physical properties of P and BM $SrCoO_{3-\delta}$ are thus dramatically different: P $SrCoO_3$ is an opaque metallic ferromagnet (F) with a Curie temperature (T_C) of ∼305 K,[49] while BM $SrCoO_{2.5}$ is an insulating antiferromagnet (AF) with a Néel temperature (T_N) of ∼540 K[50] and a band gap that has been reported to be as high as ∼2 eV.[13] Building on the ability to thermally cycle between P and BM in thin-film perovskite cobaltites,[55,56] recent work in ionic-liquid/ion-gel/ionic-conductor-based transistors established electrical cycling (i.e., gating) between these phases.[11−14,16,19−21,24−27,31] As illustrated in Figure 1(b), ionic-liquid/gel-based transistors achieve reduction of P $SrCoO_{3-\delta}$ to BM $SrCoO_{2.5}$ under positive V_g (left panel), and oxidation of BM $SrCoO_{2.5}$ to P $SrCoO_{3-\delta}$ under negative V_g (right panel),[11−14,16,19−21,24−27,31] the requisite O for the latter likely deriving from electrochemical splitting of H_2O in the ionic liquids/gels.[2,4,13,19] This cycling is nonvolatile, and intrinsically power-efficient due to low electrochemical gate current (I_g). Related effects have also been proposed for topotactic resistive random access memory devices.[57,58]

By the above means, electrochemical gating of epitaxial films of compounds such as $SrCoO_{3-\delta}$,[11−14,16,19−21,24−27,31] $SrCo_{1-x}Fe_xO_{3-\delta}$,[19] and $La_{1-x}Sr_xCoO_{3-\delta}$[18,22,23,29] has been intensively studied. In terms of the structure, both ex situ and operando studies of V_g-controlled P ↔ BM transformations have been performed, via transmission electron microscopy[14,21,22,24,27,29] and X-ray diffraction (XRD),[11−13,16,18−24,27,29] significantly advancing the understanding of this (first-order[18]) topotactic transition.[18,56,59] Interestingly, some studies, particularly on $SrCoO_{3-\delta}$, present clear evidence for tristate gating between P $SrCoO_{3-\delta}$, BM $SrCoO_{2.5}$, and hydrogenated $HSrCoO_{2.5}$,[13,25,31] while others, particularly on $La_{1-x}Sr_xCoO_{3-\delta}$, evidence bistate gating between P and BM phases;[18,22,23,29] this difference is not yet understood. In terms of electronic transport, accompanying V_g-induced metal−insulator transitions have been observed through temperature (T)-dependent resistivity (ρ) measurements,[13,18,21,23] leading to room-temperature ρ modulations up

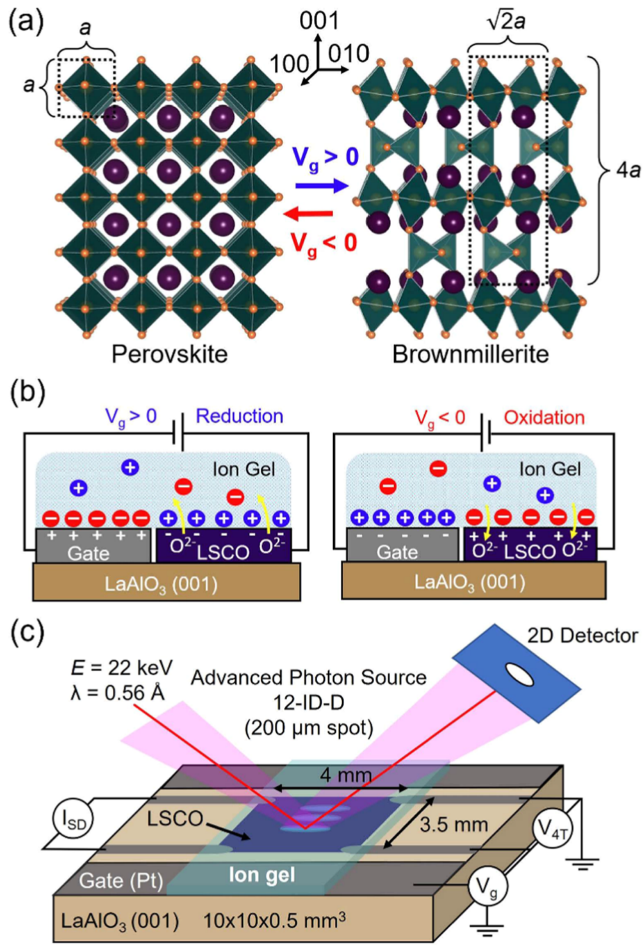

Figure 1. Crystal structure, device, and experimental setup schematics. (a) Crystal structures of LSCO in perovskite (P, left) and brownmillerite (BM, right) phases. Purple spheres are La/Sr ions, gold spheres are O ions, and the CoO_6 octahedra and CoO_4 tetrahedra are shown in green. Note the quadrupling of the c-axis lattice parameter in the BM phase due to the O vacancy order. (b) Schematic LSCO-based ion-gel-gate electrochemical transistor operating in both reduction ($V_g > 0$, left) and oxidation ($V_g < 0$, right) modes. (c) Schematic experimental device setup showing the $LaAlO_3$ substrate (which was 10 × 10 mm^2 for X-ray measurements only), LSCO channel, ion gel, Pt gate and film electrodes, incoming/outgoing synchrotron X-ray beam, source−drain current (I_{SD}), measured voltage for four-terminal measurements (V_{4T}), and gate voltage (V_g).

to 10^5 in $SrCoO_{3-\delta}$ and $La_{1-x}Sr_xCoO_{3-\delta}$.[13,18,29] In terms of thermal transport, substantial recent attention has focused on electrochemically gated cobaltite films,[23,25] with the room-temperature modulation of thermal conductivity reaching a factor of ∼10 between P $SrCoO_{3-\delta}$ and $HSrCoO_{2.5}$,[25] and a factor of ∼5 between P $La_{0.5}Sr_{0.5}CoO_{3-\delta}$ and BM $La_{0.5}Sr_{0.5}CoO_{2.5}$.[23] In terms of magnetism, a F to non-F transition is established to accompany the V_g-induced P to BM and metal−insulator transitions in $SrCoO_{3-\delta}$[13,16,19−21,31] and $La_{1-x}Sr_xCoO_{3-\delta}$,[18,22] enabling modulations of F magnetization over 2.2 μ_B/Co,[13,18] modulations of T_C over 220 K,[13,18] and room-temperature ON/OFF control of F order in $SrCo_{1-x}Fe_xO_{3-\delta}$.[19] In terms of optical properties, opaque−transparent cycling in the visible region is well-established via V_g-based P ↔ BM cycling in $SrCoO_{3-\delta}$.[13,16,31] Recent work on $La_{1-x}Sr_xCoO_{3-\delta}$ reported a more comprehensive assessment of

https://doi.org/10.1021/acsami.4c01336
ACS Appl. Mater. Interfaces 2024, 16, 19184−19197

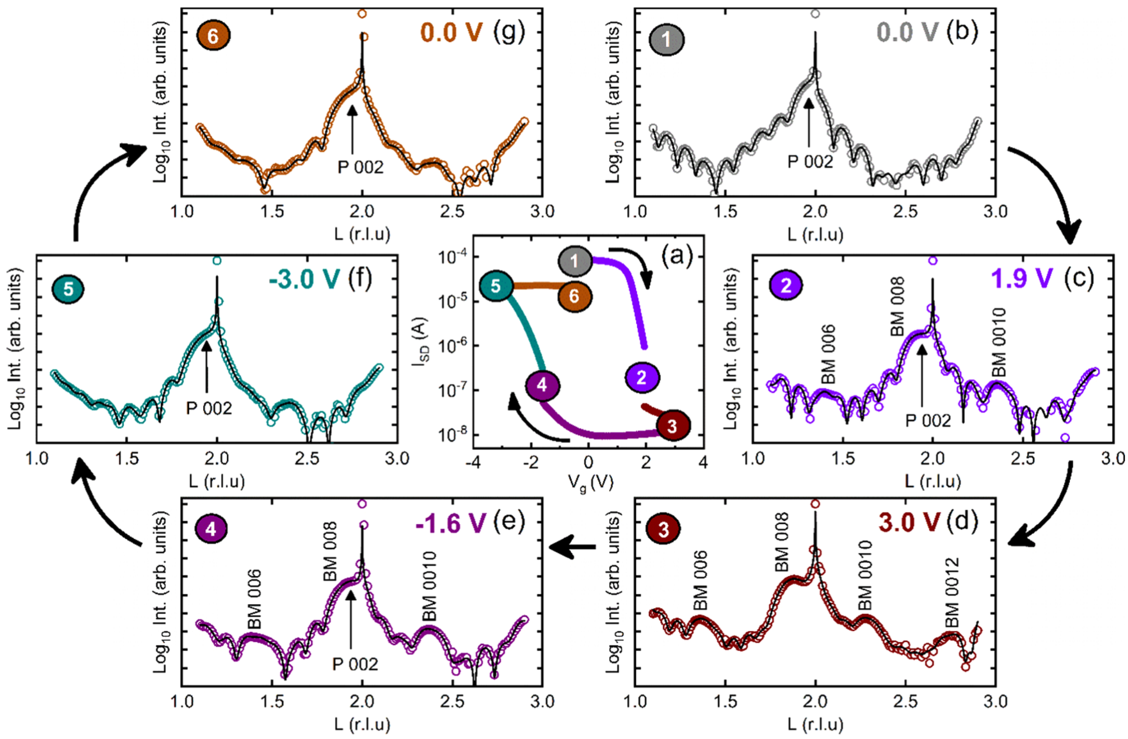

Figure 2. Perovskite ↔ brownmillerite cycling probed via gate-voltage hysteresis loops and operando SXRD. (a) Log_{10}-scale source−drain current (I_{SD}) vs gate-voltage (V_g) hysteresis loop from an ion-gel-gated 10-unit-cell-thick LSCO film. Gating was performed at 300 K, in N_2, at a sweep rate of 1 mV s^{-1} and a source−drain voltage of 0.1 V. The colored and numbered circles represent points where the V_g sweep was paused, the device was cooled to 150 K, and SXRD scans were collected; the device was then warmed to 300 K and the process repeated. (b−g) Operando specular (00*L*) SXRD scans around the $LaAlO_3$ substrate 002 reflections at Points 1−6 labeled in panel (a); these correspond to V_g = 0.0, 1.9, 3.0, −1.6, −3.0, and 0.0 V. Open circles are data points, while the solid lines are refinements. Perovskite (P) and brownmillerite (BM) peaks are labeled. Reciprocal lattice units (r.l.u.) are based on the substrate. Black arrows illustrate the sweep direction.

V_g-control over the visible to mid-infrared response, establishing promising modulations of the real and imaginary refractive index of up to ∼1.8 and 8.2, respectively.[29] Finally, in terms of translation to device applications, several advances are particularly noteworthy, including progress with P ↔ BM switching speed in $La_{0.5}Sr_{0.5}CoO_{3-\delta}$,[22] room-temperature magnetoionic function in $SrCo_{1-x}Fe_xO_{3-\delta}$,[19] low-power nonvolatile modulation of *x*-dependent optical properties in $La_{1-x}Sr_xCoO_{3-\delta}$,[29] and strain- and doping-based tuning of P → BM threshold voltages in $La_{1-x}Sr_xCoO_{3-\delta}$, with excellent room-temperature stability.[18]

While the above progress is impressive, a shortcoming of the existing literature is the heavy focus on P and BM end points. Studies exist of structural evolution as a quasi-continuous function of gating time or voltage,[11−14,16,18,19,21,23,24] with accompanying tracking of transport[13,14,16,18,23,24] and magnetic[16,18,19] properties, but V_g hysteresis loops of essential quantities such as I_{SD} (the source−drain current), I_g, ρ, lattice parameters, other structural parameters, etc., are rarely, if ever, reported,[20,24,26,27] though they have proven insightful in other systems.[60] This omission is glaring, for many reasons. First, hysteresis loops are an obvious base for frequency-dependent measurements to probe and advance the limits on cycling speed of V_g-driven redox-based control. Second, the same can be said for the other main obstacle to applications, namely, endurance, particularly at high cycle numbers. Third, there exist powerful methods for the study of hysteretic phenomena, such as minor hysteresis loops[61,62] and first-order reversal curves,[63−65] which have much potential to advance the understanding of topotactic V_g-driven P ↔ BM cycling, but have not yet been applied.

The critical application issue of cycling speed also highlights another shortcoming of the existing literature, specifically the dearth of studies on ultrathin films. It is apparent that the switching speed of redox-based V_g-cycled devices will be limited by diffusion of the relevant species, in the cobaltite P ↔ BM case the D_{V_O} at (ideally) ambient temperature.[2,4] This directly focuses interest on ultrathin cobaltite films in such devices, but this is not prevalent in the literature. Early reports focused on 20−50-nm-thick films,[11,13,14] reducing to 11 nm in $La_{1-x}Sr_xCoO_{3-\delta}$[18] and 5 nm in a single report on $SrCoO_{3-\delta}$,[27] typically well above the unit-cell-level thickness to which perovskite oxide heterostructures are explored in other contexts.[66] It is thus unknown how P ↔ BM ionic control is affected by interface/surface effects and dimensional confinement in the ultrathin limit.

In light of the above, here, we report the first complete study of hysteresis and reversibility across the V_g-controlled P ↔ BM transformation, using ion-gel-gated ultrathin (10-unit-cell-thick (3.8 nm)) epitaxial films of $La_{0.5}Sr_{0.5}CoO_{3-\delta}$ (hereafter, LSCO) on $LaAlO_3$ (LAO) (001) substrates. I_{SD} vs V_g hysteresis loops are shown to reveal a wealth of new mechanistic findings, including asymmetric redox kinetics due to differing oxygen diffusivities in the P and BM phases, nonmonotonic P ↔ BM transformation rates due to the first-order nature of the topotactic transformation, and limits on first-cycle reversibility. Simultaneous operando synchrotron XRD (SXRD) coupled with quantitative depth-wise structural

https://doi.org/10.1021/acsami.4c01336
ACS Appl. Mater. Interfaces 2024, 16, 19184−19197

refinement further elucidates these findings, in particular, establishing the origins of the limits on first-cycle reversibility in terms of structural degradation and roughening. Bringing to bear powerful approaches to the study of hysteretic phenomena, minor hysteresis loops are shown to provide much additional insight, enabling the first rational design of an optimal V_g cycle. Finally, these advances are combined to present state-of-the-art V_g cycling of electronic/magnetic properties in electrolyte-gated LSCO, including $>10^5$ I_{SD} ON/OFF ratios at room temperature, and reversible metal−insulator−metal and F−non-F−F cycling. This is all achieved in 10-unit-cell-thick LSCO, setting the stage for future work to address the critical application issues of the ultimate limits on frequency and endurance.

■ RESULTS AND DISCUSSION

As already noted, Figure 1(a,b) presents schematics of the P and BM crystal structures of LSCO and the principle of operation of ion-gel-gated LSCO thin-film electrochemical transistors. As in SCO, electrochemical splitting of residual H_2O in the ion gels is believed to play a key role in the redox switching from P to BM and particularly BM to P.[2,4,13,19] Figure 1(c) provides additional details on the experimental setup, showing the device geometry, electrical wiring for transport measurements, and configuration for operando SXRD. Fabrication and measurement details are provided in the Methods section. These devices are based on high-quality, epitaxial, single-phase, smooth LAO/LSCO(10-unit-cell) films that have been extensively characterized;[18,23,29,67−70] their electronic/magnetic properties are among the best reported[67−70] at this thickness and strain state (1.2% compression). Importantly, LSCO films are in the P phase as-deposited,[18,22,23,29] in contrast to $SrCoO_{3-\delta}$ gating studies, which start from as-deposited BM[11−14,16,19−21,24−27,31] due to the difficulty of stabilizing P $SrCoO_{3-\delta}$ under typical growth conditions.[55,71] We estimate an initial $\delta \approx 0.14$ for these P LSCO films, using established methods based on comparisons of resistivity to bulk single crystals.[68]

We begin the discussion of the primary results and analyses with Figure 2(a), which shows a 300 K $I_{SD}-V_g$ hysteresis loop for an ion-gel-gated 10-unit-cell LAO/LSCO film. This loop was recorded at a slow V_g sweep rate of 1 mV s^{-1} but was interrupted at the numbered points to record operando SXRD data. As discussed below, uninterrupted constant-sweep-rate loops provide substantial finer detail, but Figure 2(a) nevertheless serves as a good starting point to discuss initial observations. The loop starts (Point 1) at $V_g = 0$, in the as-deposited P phase, where I_{SD} at this source−drain voltage (0.1 V, see the Methods section) is $\sim 1 \times 10^{-4}$ A. More extensive four-terminal transport data are discussed below, but we note for now that this corresponds to $\rho \approx 300$ $\mu\Omega$ cm at 300 K, representative of high-quality 10-unit-cell LAO/LSCO films.[67−70] As V_g is increased, a reasonably well-defined threshold voltage of ∼1 V is apparent,[18] above which I_{SD} drops rapidly by orders of magnitude, before slowing at ∼2 V (Point 2). I_{SD} then flattens by 3 V (Point 3), at which stage the V_g sweep direction was reversed. A more gradual increase of I_{SD} is observed at negative V_g (centered on ∼ −2 V), followed by saturation at −3 V (Point 5). Notably, returning V_g to zero (Point 6) results in substantially recovered I_{SD} but not to exactly the initial level (Point 1). Quantitatively, the ON/OFF I_{SD} ratio of this device on gating P → BM (at positive V_g) is $\sim 9 \times 10^3$, whereas the ON/OFF I_{SD} ratio on gating BM → P (at negative V_g) is $\sim 2 \times 10^3$, meaning that there is a factor of ∼4 difference in I_{SD} between the initial (Point 1) and final (Point 6) states. As returned to below, this factor is only ∼2 for ρ, meaning that a significant part of I_{SD} decrease from Point 1 to Point 6 is contact-related.

SXRD data at Points 1−6 around the loop in Figure 2(a) confirm that the above behavior results from P → BM → P cycling and clarifies the origin of the loop nonclosure. Figure 2(b−g) shows specular (00*L*) SXRD scans centered on the LAO(002) reflection, i.e., $\log_{10}$ intensity vs *L* in substrate reciprocal lattice units (r.l.u.). At Point 1 (Figure 2(b)), SXRD confirms high-quality smooth LAO(001)/LSCO. The primary reflection is just to the left of the LAO(002) substrate, corresponding to an out-of-plane lattice parameter $a = 3.89$ Å, in good agreement with the 1.2% mismatch and LSCO Poisson ratio of ∼1/3.[69,70] Laue fringes are pronounced, consistent with high structural quality and low surface/interface roughness. By Point 2 at 1.9 V, however (Figure 2(c)), the situation changes: The LSCO reflection near the substrate downshifts (indicating lattice expansion, consistent with V_O formation[18,72]), while clear BM 006 and 0010 peaks emerge, indicating the quadrupling of the *c*-axis lattice parameter in the BM phase. The broad primary reflection in fact appears to have both P 002 and BM 008 components, consistent with prior observation of P/BM coexistence at intermediate voltages, implying a first-order transition.[18] By Point 3 (3.0 V, Figure 2(d)), only BM 006, 008, 0010, and 0012 peaks are apparent, indicating nominally phase-pure BM. Figure 2(e) at Point 4 then shows that the BM is retained at −1.6 V, albeit with an upshift of the primary reflection, consistent with V_O annihilation. In contrast, at Points 5 and 6 in Figure 2(f,g) (−3.0 and 0.0 V, respectively), the primary features of BM are removed, leaving essentially the P 002 and associated Laue fringes. The SXRD data at Points 1−6 are thus qualitatively consistent with an interpretation of the hysteresis loop in Figure 2(a) in terms of P → BM → P cycling, with P/BM phase coexistence at intermediate points. As an aside, we note that the BM in Figure 2(c−e) is (00*L*)-oriented, i.e., the alternating octahedral and tetrahedral Co−O layers (Figure 1(a)) are in-plane. This is as in our prior work,[18] independent of the strain state and V_g cycling; this is in contrast to some observations[21] for reasons that are not entirely clear. Also, as noted in the Introduction section, no clear evidence of H incorporation or a $HLa_{0.5}Sr_{0.5}CoO_{2.5}$ phase is found, and the origin of this difference compared to the $SrCoO_{3-\delta}$ system remains unclear.

Regarding the loop nonclosure in Figure 2(a), i.e., the inequivalence of Points 1 and 6, it is noteworthy that the SXRD scans in Figure 2(b,g) are different. The primary LSCO P 002 reflection in Figure 2(g) is broader and less intense than in Figure 2(b), and the Laue fringes are less pronounced and wider-spaced. This immediately suggests that the high epitaxial quality in the as-deposited P state is reduced after the first P → BM → P cycle. Although the P ↔ BM transformation is topotactic, this is perhaps unsurprising. Deeper insight is provided by quantitative analysis of SXRD data. This was achieved through a structural refinement based on a newly developed constrained-phase-retrieval algorithm, as described in Methods and Supporting Information Section A. This procedure refines the one-dimensional, laterally averaged, layer-by-layer electron density profile as a function of depth through the film and substrate. Example refinements are shown in close-up in Figure 3(a) for the $V_g = 0$ (as-deposited), 3.0,

https://doi.org/10.1021/acsami.4c01336
ACS Appl. Mater. Interfaces 2024, 16, 19184−19197

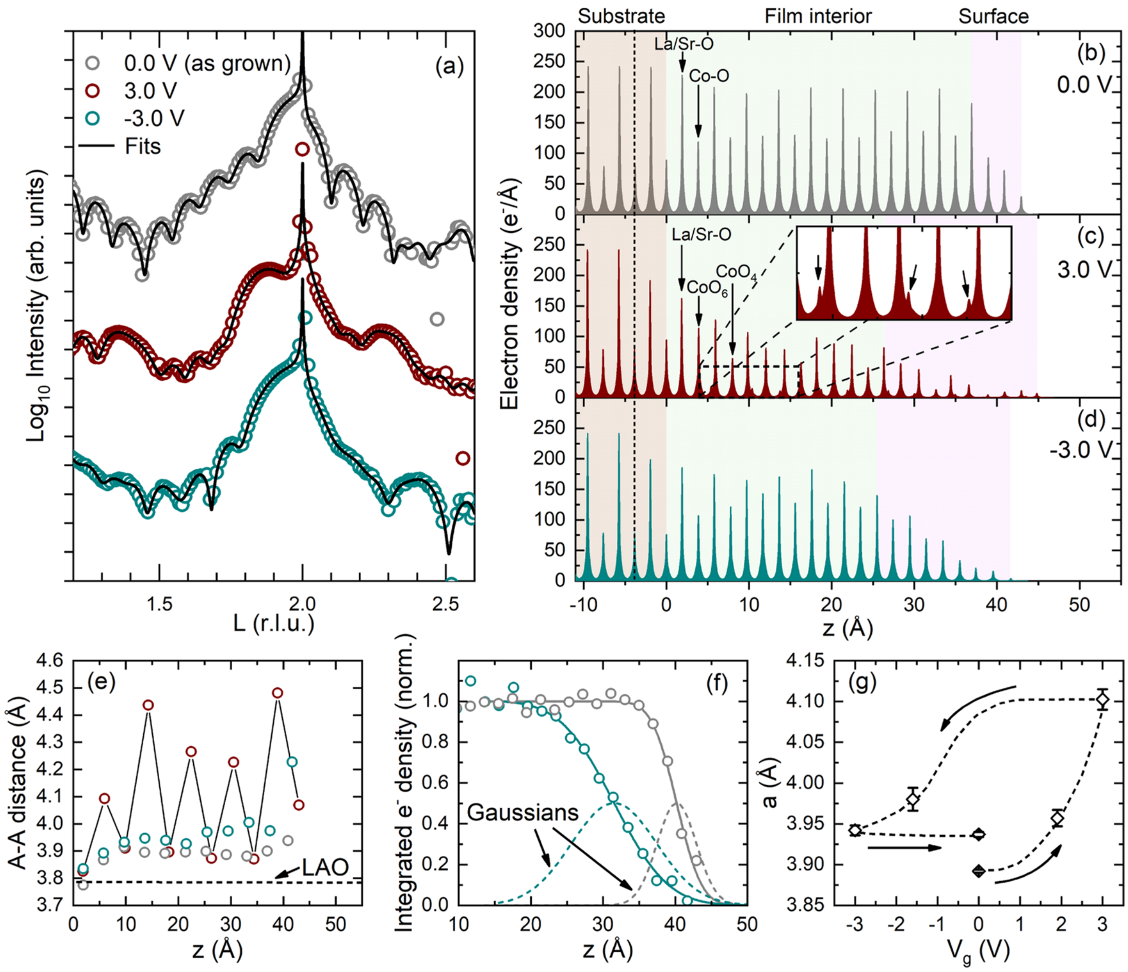

Figure 3. Structural details around perovskite ↔ brownmillerite hysteresis loops from quantitative operando SXRD. (a) Operando SXRD data (open points) and refinements (black lines) at selected gate voltages (V_g): 0.0 V (as-deposited, gray), 3.0 V (maroon), and −3.0 V (green), as in Figure 2(b,d,f). Reciprocal lattice units (r.l.u.) are based on the substrate. (b−d) Electron density vs depth (z) profiles extracted from the refinements in panel (a), at 0.0 V (as-deposited, gray), 3.0 V (maroon), and −3.0 V (green). The substrate (light brown), LSCO film interior (light green), and LSCO film surface region (pink, from the first atomic plane above which significant drops in electron density occur) are labeled, and the vertical dashed line marks the start of the refined range. In the LSCO, the more intense peaks are the La/Sr−O layers, while the less intense peaks are Co−O layers (the integrated peak intensities correspond to the electron densities on each layer). The inset in panel (c) highlights the features due to brownmillerite. (e) Depth dependence of the A-site-to-A-site vertical distance extracted from panels (b−d), using the same V_g color scheme. The dashed line corresponds to the substrate ($LaAlO_3$ (LAO)) value. (f) Integrated electron (e^-) density (normalized to 1 in the film interior) vs. depth (z) for the 0.0 V (as-deposited perovskite) and −3.0 V (gated back to perovskite) cases. The solid lines are error function fits, while the dashed curves are corresponding normalized Gaussian distributions of film thickness illustrating the different surface locations and roughness. (g) Extracted film-interior out-of-plane lattice parameter (a) vs V_g. Black arrows illustrate the sweep direction and the dashed line is a guide to the eye. The error bars represent the standard deviation of the mean value of the A-site-to-A-site distance in the film interior.

and −3.0 V cases, as in Figure 2(b,d,f), respectively. The open points here are data and the solid lines are refinements, which describe the data very well (as in Figure 2(b−g)). Figure 3(b−d) shows the corresponding extracted depth (z) profiles of electron density. At V_g = 0 (Figure 3(b)), the determined structure is near-ideal, with a quite sharp LAO/LSCO interface, uniform electron density in the LSCO interior (with alternating La/Sr−O and Co−O layers), and a low-roughness top surface. The extracted root-mean-square (rms) roughness is 2.7 ± 0.3 Å, resulting in a surface region (pink background in Figure 3(b−d), shown as the first atomic plane above which a significant drop in electron density occurs) of ∼2 unit cells.

At V_g = 3.0 V (Figure 3(c)), as expected, the refined depth profile is much different. First, the electron densities of the atomic planes in the film interior are distinctly suppressed relative to Figure 3(b), and a subtle two-peak structure develops on the La/Sr−O planes (inset to Figure 3(c)). We ascribe the overall electron density decrease to diminished structural coherence of the BM phase relative to the as-deposited P film, likely due to formation of multiple coexisting BM domains during topotactic reduction. The two-peak structure in the inset is expected in BM due to the noncoplanar O^{2-} ions (Figure 1(a)). Associated with this, the inter-A-site distance oscillates vs depth, due to the alternating octahedrally and tetrahedrally coordinated Co−O layers.[50,53,54] This is shown in Figure 3(e), where the depth profile of the A−A distance clearly oscillates in the V_g = 3.0 V (i.e., BM) case, in contrast with the V_g = 0 and −3.0 V (i.e., P) cases. In the latter cases, there is only a weak increase in A−A distance toward the surface, potentially reflecting a mild composition gradient. The conclusion of nominally phase-pure BM at 3.0 V is thus

https://doi.org/10.1021/acsami.4c01336
ACS Appl. Mater. Interfaces 2024, 16, 19184−19197

supported by not only the BM peaks in Figures 2(d) and 3(a) but also the details of the depth profile. Another observation from the V_g = 3.0 V data (Figure 3(c)) is that the LSCO surface roughness is higher in the BM phase. The rms surface roughness in fact increases to 6.7 ± 1.2 Å, generating a surface region (pink background) of ∼4 pseudocubic unit cells. Finally, we note that some of the findings at 3.0 V depend on an assumption in the refinement, specifically whether the first LSCO layer (at the substrate interface) is octahedral or tetrahedral Co−O. Based on prior literature,[73,74] we assume octahedral CoO_6; the impact of this is explored in Supporting Information Section B, Figure S1.

Figure 3(d) moves to V_g = −3.0 V, in the recovered P state, revealing several differences from the as-deposited P state (Figure 3(b)). First, the electron density in the LSCO interior, particularly on La/Sr−O planes, does not fully recover after the BM → P transformation, very likely reflecting that oxidation from the multidomain BM state results in a lower structural coherence P phase compared to the as-deposited one. Second, there are striking changes near the surface. The surface region (pink background in Figure 3(d)) not only broadens relative to Figure 3(b) but also shifts to lower *z*, indicating decreased thickness. This is illustrated in Figure 3(f), where the integrated electron density of each atomic layer is plotted (normalized to the interior) vs *z*, comparing the V_g = 0 and −3.0 V cases. P → BM → P cycling is seen to decrease the thickness from 40.2 to 31.5 Å, simultaneously increasing the rms roughness from 2.7 ± 0.3 to 5.9 ± 0.4 Å. These points are further emphasized by the solid lines in Figure 3(f), which show normalized Gaussian distributions of thickness based on the shown density profiles at 0 and −3.0 V (more details are provided in Supporting Information Section B, Figure S2). The ∼2 unit-cell decrease in LSCO thickness may seem surprising, but is likely simply due to mild etching at large positive V_g; this is known in electrolyte gating,[67,75,76] including oxides[67,76] and LSCO,[67] the latter having been studied via atomic force microscopy to the point of etch pit formation. This is thought to be due to electrochemical splitting of residual H_2O in ionic liquids/gels, generating H^+ ions that acid-etch the film at large positive V_g, decreasing the thickness and increasing the roughness.[67] Such effects are more noticeable here in very thin films compared to the majority of literature studies at 10−50 nm.

As a final finding from operando SXRD, Figure 3(g) shows the extracted out-of-plane lattice parameter around the first P → BM → P cycle. As noted in connection with Figure 1(b), the V_g = 0 as-deposited *a* = 3.89 Å is as-expected based on the strain state on LAO.[18,23,69,70,72] As V_g is increased, V_O formation leads to *a* rapidly increasing above ∼1 V, reaching 4.10 Å at 3.0 V in the BM phase, consistent with a prior work.[18] (This is a pseudocubic lattice parameter here, i.e., 1/4 of the BM out-of-plane lattice parameter.) Decreasing V_g then decreases *a* due to V_O annihilation, reaching $a \approx 3.94$ Å in the recovered P phase at −3.0 and 0 V. The slight (1.2%) difference in lattice parameters between the as-deposited and recovered P states is consistent with the above findings, highlighting that, in addition to the lower structural quality than the as-deposited film, the δ of the cycled P film is also slightly larger. Based on the known $a(\delta)$ in the P phase of LAO/LSCO,[18,68,72] we estimate a final δ of 0.19 compared to the initial 0.14 (see Supporting Information Section B, Figure S3, and Table S1, for more details). The loop nonclosure in Figure 2(a) thus results from a combination of factors in the cycled P film, including slightly larger δ, reduced structural coherence, and increased roughness. Limits on the oxidation of the recovered P phase have been uncovered in prior thermal cycling studies also.[77]

With the main features of the I_{SD} vs V_g hysteresis loop in Figure 2(a) understood in terms of structural insights from quantitative operando SXRD, we turn to additional insights revealed by uninterrupted constant-sweep-rate hysteresis loops. Figure 4(a) shows a typical loop, recorded at 300 K, 1 mV s^{-1} sweep rate, and 0.1 V source−drain voltage. Similar to Figure 2(a), I_{SD} starts at $\sim 1 \times 10^{-4}$ A in the as-deposited P phase; this corresponds to $\rho \approx 300$ $\mu\Omega$ cm at 300 K (and $\rho \approx 150$ $\mu\Omega$ cm at 10 K), representative of high-quality 10-unit-cell LAO/LSCO.[67−70] While the main features of Figure 2(a) are retained in Figure 4(a), such as the clear P → BM and BM → P transitions (at positive and negative V_g, respectively), and the loop nonclosure, interesting new features emerge in constant-sweep-rate loops. First, the P → BM transformation at positive V_g completes more abruptly (between ∼1.5 and ∼2.5 V) than the BM → P transition at negative V_g (between ∼0.5 and ∼−2.5 V), leading to distinctly asymmetric loops. Second, there emerge obvious shelf features on the right and left sides of the

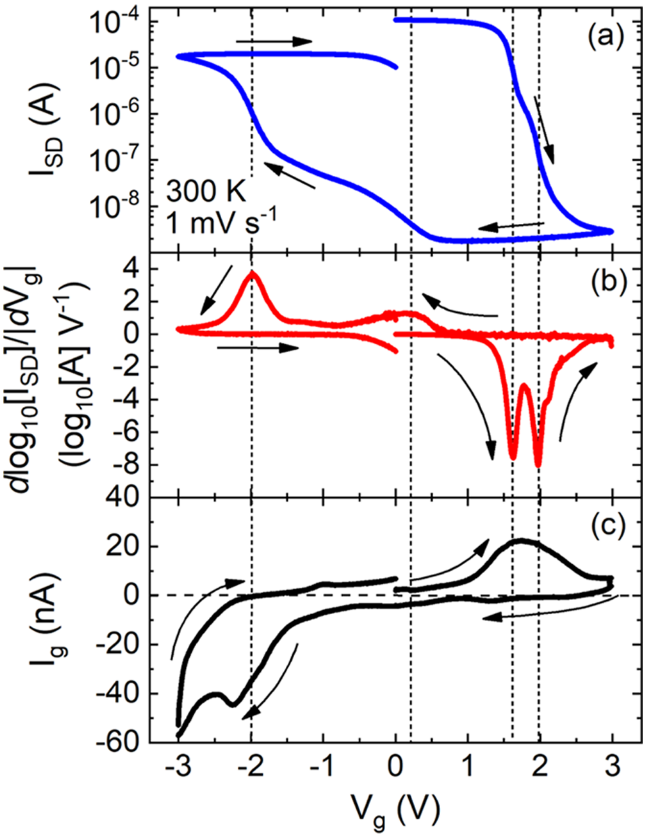

Figure 4. Detailed gate-voltage hysteresis loops around the perovskite ↔ brownmillerite transformation. (a) Log_{10}-scale source−drain current (I_{SD}) vs gate-voltage (V_g) hysteresis loop from an ion-gel-gated 10-unit-cell-thick LSCO film. Gating was performed at 300 K, in vacuum (<1 × 10^{-5} Torr), at a sweep rate of 1 mV s^{-1}, and a source−drain voltage of 0.1 V. (b) Corresponding logarithmic derivative of I_{SD} vs V_g, i.e., $d\log(I_{SD})/|dV_g|$. (c) Corresponding gate current (I_g) vs V_g. Black arrows illustrate the sweep direction. Vertical dashed lines mark the features in the data described in detail in the text.

https://doi.org/10.1021/acsami.4c01336
ACS Appl. Mater. Interfaces 2024, 16, 19184−19197

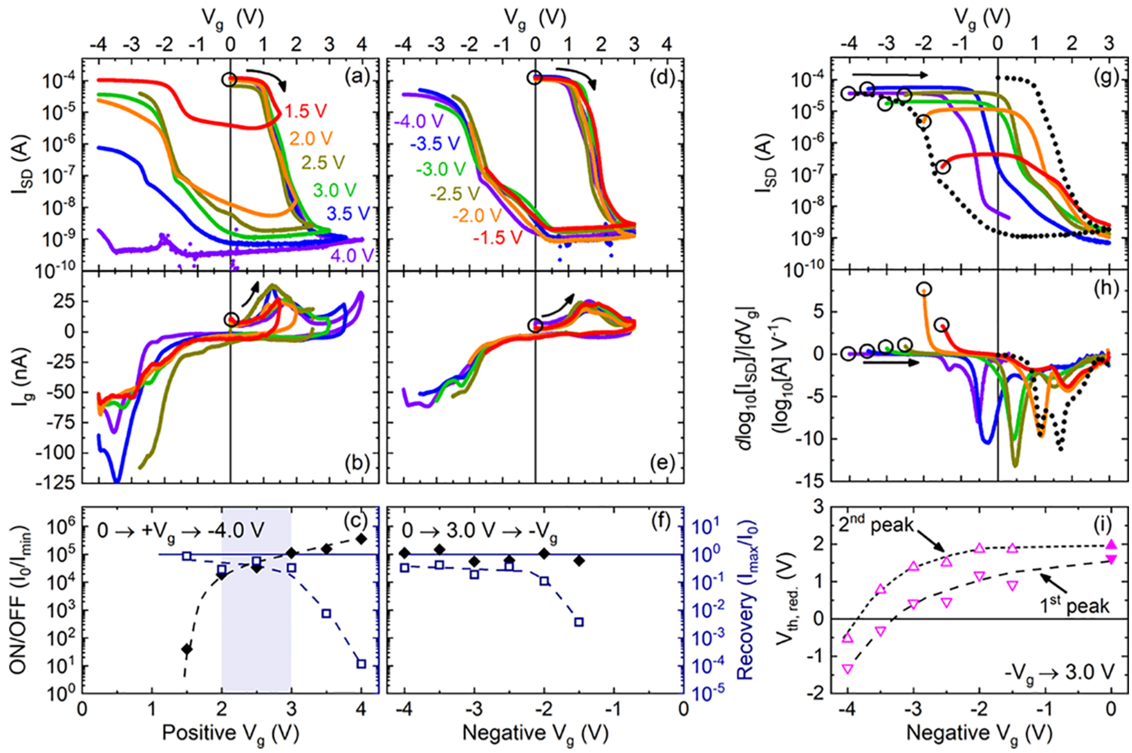

Figure 5. Minor hysteresis loops: designing an optimal gate-voltage cycle. (a−c) Minor hysteresis loops with fixed minimum (negative) gate voltage (−4.0 V) but varied maximum (positive) gate voltage (1.5−4.0 V, in varied colors). Plotted are the gate-voltage (V_g) dependences of (a) source−drain current (I_{SD}) on a $\log_{10}$ scale, (b) gate current (I_g), and (c) current ON/OFF ratio (black, left axis) and current recovery ratio (blue, right axis). (d−f) Minor hysteresis loops with fixed maximum (positive) gate voltage (3.0 V) but varied minimum (negative) gate voltage (−1.5 to −4.0 V, in varied colors). Plotted are the V_g dependences of (d) I_{SD} on a $\log_{10}$ scale, (e) I_g, and (f) the current ON/OFF ratio (black, left axis) and current recovery ratio (blue, right axis). The ON/OFF ratio is defined as I_0/I_{min}, where I_0 is the initial ($V_g = 0$) value of I_{SD}, and I_{min} is the minimum value (at any $V_g > 0$) of I_{SD}. The recovery ratio is defined as I_{max}/I_0, where I_0 is the initial ($V_g = 0$) value of I_{SD}, and I_{max} is the maximum value (at any $V_g < 0$) of I_{SD} after cycling from positive to negative V_g. (g, h) Increasing V_g sweeps (varied colors) after sweeping from 0 to 3.0 V, to varied negative voltages. Plotted are the V_g dependences of (g) I_{SD} on a $\log_{10}$ scale and (h) $d\log(I_{SD})/|dV_g|$. The dotted black line is a major hysteresis loop for reference. Shown in panel (i) are the dependences of the threshold voltages for reduction ($V_{th,red}$), defined by the peaks in panel (h), on the magnitude of the minimum (negative) gate voltage. All data were taken at 300 K, in vacuum (<1 × 10^{-5} Torr), at a sweep rate of 1 mV s^{-1}, and a source−drain voltage of 0.1 V. Black circles and arrows indicate the starting points of the highlighted loops and the sweep directions, respectively. In panels (c, f), the blue horizontal lines mark ideal recovery, i.e., a recovery ratio of 1.

loop, which are sharp on the right and broader on the left. Along with these unusual features, the peak ON/OFF I_{SD} ratio reaches almost 10^5, comparable to the best reported in electrochemically gated cobaltites.[13,18,21,22,29] Figure 4(b) highlights and quantifies these observations by plotting the V_g dependence of a logarithmic derivative of I_{SD}, i.e., $d\log_{10}(I_{SD})/|dV_g|$. This reveals two sharp, closely spaced negative peaks at positive V_g, along with two broader, further-spaced positive peaks at negative V_g. The minima in the logarithmic derivative between these peaks reflect the shelf features in Figure 4(a), while the larger spacing between the peaks at negative V_g reflects the asymmetry in Figure 4(a). The corresponding $I_g(V_g)$ loop in Figure 4(c) reveals a broad positive-V_g peak centered on the two sharp peaks in the logarithmic derivative in Figure 4(b), along with two broader negative-V_g peaks aligned with the broader peaks in the logarithmic derivative in Figure 4(b). The alignment of these features is highlighted by the vertical dotted lines in Figure 4. In Figure 4(c), the features are superimposed on the typical increases in the magnitude of I_g at the extremes of V_g (particularly negative V_g), which indicate the approach to the limits of the electrochemical stability window.[1,2]

Based on the current understanding of the voltage-driven P → BM → P topotactic phase transformation in gated cobaltite films, we provide simple interpretations of the phenomena in Figure 4. First, we believe that the distinct V_g asymmetry in Figure 4(a,b) simply reflects the known differences in mass transport dynamics between P → BM and BM → P transformations.[59] Due to the one-dimensional V_O channels in the O-deficient planes of BM LSCO (Figure 1(a)),[50,53,54] the dimensionality for O diffusion is distinctly reduced compared to the three-dimensional situation in V_O-disordered P LSCO. Consequently, the kinetics of the oxidative transformation from BM to P should be slower than the reductive transformation from P to BM, which we propose results in the V_g asymmetry in Figure 4(a,b). Both experimental and theoretical literature support this interpretation. X-ray photon correlation spectroscopy on thermally transforming $SrCoO_{3-\delta}$, for example, evidences one-dimensional ionic migration processes from BM → P, in contrast to three-dimensional processes from P → BM.[59] Calculations of activation energies for migration of O defects also yield minimum values of only 0.5−0.6 eV in the P phase of $SrCoO_{3-\delta}$, compared to a more anisotropic 0.6−0.8 eV in the BM phase.[43,78] From the applications perspective, such factors likely mean that the BM → P transformation will limit the ultimate frequency of P → BM → P cycling.

https://doi.org/10.1021/acsami.4c01336
ACS Appl. Mater. Interfaces 2024, 16, 19184−19197

Second, with respect to the shelf features in Figure 4(a) that generate the split peaks in Figure 4(b), we believe the key factor is the first-order nature of the P ↔ BM transformation.[18,56,59] Specifically, we interpret these features not as twin peaks per se, but in terms of a region of anomalously low transformation rate in the middle of the transformation. We believe this occurs as the system enters the P/BM coexistence regime, where additional work must be done to propagate P/BM phase boundaries before a single-phase state can be reached. Using positive V_g as an example, reduction commences at 1.0−1.5 V in Figure 4, with the formation of V_O in the P phase, reaching a maximum transformation rate shortly thereafter. At this point, BM regions appear, resulting in P/BM coexistence, slowing the transformation due to the work needed to propagate P/BM boundaries to expand the BM domains. As these boundaries are extinguished, and phase-pure BM is approached, the transformation rate again peaks before the final stage of reduction and V_O ordering in phase-pure BM. These processes occur in reverse at negative V_g, but with smaller, broader, wider-spaced peaks in Figure 4(b) due to the abovementioned asymmetry in D_{V_O} in P and BM phases. Similar features then arise in Figure 4(c), particularly peaks in the electrochemical gate current when the P ↔ BM transformation rates peak, analogous to other redox-based gated devices.[60] Such details of the P ↔ BM transformation mechanism in electrolyte-gated cobaltite films have not been previously detected, highlighting the power of V_g hysteresis loops.

Reassuringly, the data of Figure 4(c) are also in reasonable quantitative consistency with the expected redox mechanism. Integrating the raw data of I_g vs time corresponding to the positive-V_g peak in Figure 4(c), for example, generates a charge value that is only a factor of ∼2 larger than expected based on removal of a half an oxygen per unit cell on transforming from P to BM (based on known film area and thickness). This is a reasonable level of agreement considering that a more accurate analysis would require subtraction of effects associated with ionic motion in the ion gel and water splitting. While we emphasize in the Introduction section the voltage-driven nature of the effects studied in this work, we thus acknowledge that the quantity of gate current flowing under the applied gate voltages is of course significant and meaningful. As a final comment on the data of Figure 4, we note that additional work to measure such hysteresis loops as a controlled function of environment and humidity would be of high interest in order to further understand the role of residual H_2O. A measurement scheme with a reference electrode would be beneficial in such studies, enabling direct interpretation of the voltage scale in Figure 4(c).

As already noted, there exist a number of additional powerful methodologies to probe hysteretic phenomena in condensed matter systems, not yet applied to V_g hysteresis in these types of electrochemical transistors. Perhaps the simplest is minor hysteresis loops, which are explored in detail for ion-gel-gated LAO/LSCO(10-unit-cell) in Figure 5. Shown in Figure 5(a) is a series of 300 K minor $I_{SD}(V_g)$ loops recorded by sweeping from V_g = 0 to varied maximum positive V_g (labeled next to each curve), then back to a constant minimum V_g of −4.0 V. The first striking observation is that the curves trace essentially the same trajectory at positive V_g, exhibiting a sharp decrease beyond ∼1 V (due to reduction of P LSCO), the now familiar shelf at intermediate V_g (across the P → BM transformation) and then saturation at low I_{SD} beyond ∼3 V (the ON/OFF ratio again reaches ∼10^5 as phase-pure BM is reached). This evidences high reproducibility of these devices and hysteresis features. In stark contrast to the overlapping curves at positive V_g, the recoil trajectories when the V_g sweep is reversed depend strongly on the maximum positive V_g. When the maximum V_g is only 1.5 V, the recoil trajectory is initially roughly horizontal to ∼ −1.5 V, below which I_{SD} recovers to almost exactly its initial (V_g = 0) value. This is therefore a highly reversible cycle in terms of initial and final I_{SD}, but with an ON/OFF ratio of only 4 × 10^1, likely involving little BM formation/annihilation. As the maximum V_g is increased to 2.0−3.0 V, somewhat similar behavior prevails, an initially roughly horizontal recoil trajectory occurring prior to substantial recovery of I_{SD} at negative V_g. The I_{SD} ON/OFF ratio progressively increases (to 1 × 10^5 at a maximum V_g of 3.0 V), indicating a full P → BM transition, at the cost of relatively modest decreases in recovery in terms of initial and final I_{SD}. At maximum V_g ≥ 3.5 V, however, while marginal additional gains in ON/OFF ratio are achieved, these come at the cost of dramatic decreases in recovery. By 3.5 V, for example, I_{SD} at −4.0 V reaches only 10^{-6} A, a factor of >10^2 below the initial I_{SD}. By 4.0 V maximum V_g, the recovery at negative V_g is negligible. As this progression occurs, the $I_g(V_g)$ curves (Figure 5(b)) reveal broad peaks at positive V_g centered on the P → BM transformation (as in Figure 4(c)), but with larger changes at negative V_g. Specifically, larger maximum V_g generally leads to a larger magnitude, steeper I_g at negative V_g, indicating large electrochemical currents.

Figure 5(c) summarizes these results by plotting the ON/OFF ratio (left axis, black points) and the recovery ratio (right axis, blue points) vs the maximum positive V_g applied. The ON/OFF ratio is defined as I_0/I_{min}, where I_0 is the initial (V_g = 0) I_{SD} and I_{min} is the minimum I_{SD} at positive V_g. The recovery ratio is defined as I_{max}/I_0, where I_{max} is the maximum recovered I_{SD} at negative V_g. The ideal behavior thus corresponds to the largest possible ON/OFF ratio at a recovery ratio close to unity. What is found in Figure 5(c) is instead a clear compromise. At higher maximum V_g, the ON/OFF ratio can be driven above 10^5, even approaching 10^6, but at the cost of diminishing recovery, particularly above 3 V. The light blue shaded region at 2−3 V thus defines the optimal maximum V_g, realizing ON/OFF ratios near 10^5 with recovery ratios up to ∼0.6 (60%).

Complementary to Figure 5(a), Figure 5(d) shows $I_{SD}(V_g)$ minor loops recorded with a constant maximum V_g of 3.0 V but varied minimum (negative) V_g, from −1.5 to −4.0 V. The positive V_g curves are tightly consistent, as are the corresponding I_g behaviors in Figure 5(e). The threshold, shelf, and saturation effects again arise in $I_{SD}(V_g)$, accompanied by broad peaks in $I_g(V_g)$, as explained above. Interestingly, the various traces also overlap at negative V_g, yet further evidencing the high reproducibility of these devices and hysteresis loop features. Decreasing minimum V_g thus leads to increased recovery while maintaining the 10^5 ON/OFF ratio set by the maximum V_g = 3.0 V. This is illustrated in Figure 5(f), where the recovery ratio increases as the minimum (negative) V_g is decreased, then saturates at −2.5 V. These data thus suggest that all minimum V_g values below −2.5 V result in optimal recovery to the P state. Further analysis, however, reveals another factor. Figure 5(g,h) illustrates what evolves in I_{SD} when devices are cycled from 0 to 3.0 V, to varied minimum (negative) V_g, then back to positive V_g to

https://doi.org/10.1021/acsami.4c01336
ACS Appl. Mater. Interfaces 2024, 16, 19184−19197

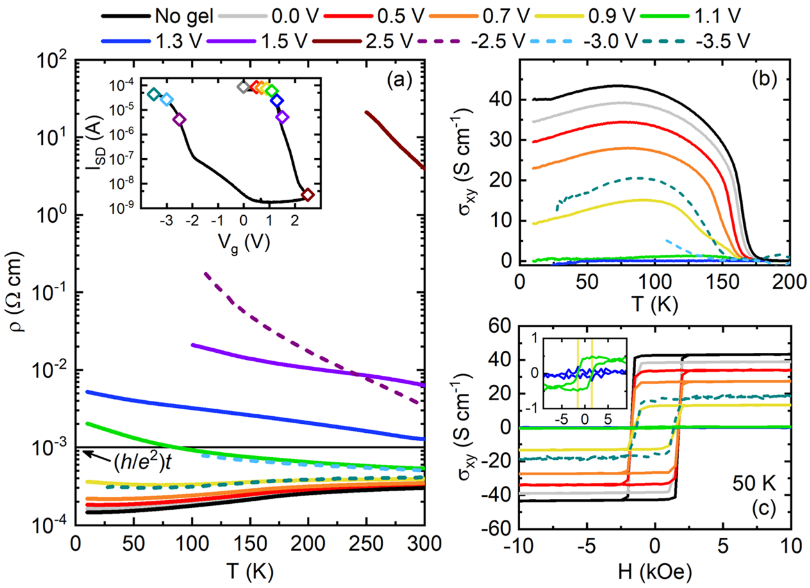

Figure 6. Reversibility of electronic and magnetic properties. (a) Temperature (T) dependence of the resistivity (ρ) of a 10-unit-cell-thick LSCO film at various gate voltages (V_g) around the 300 K hysteresis loop shown in the inset. The hysteresis loop plots the source−drain current (I_{SD}) vs V_g (solid black line), with the various V_g values in the main panel highlighted by points that are color-coded with the main panel (and defined at the top of the figure). In the main panel, solid lines are for increasingly positive V_g (P → BM), and dashed lines are for increasingly negative V_g (BM → P). The horizontal black line marks the quantum resistance multiplied by the film thickness, i.e., ht/e^2, where h is Planck's constant, e is the electronic charge, and t is the film thickness. (b) Corresponding T-dependence of the transverse (Hall) conductivity (σ_{xy}) at the same V_g as in panel (a). (c) Corresponding 50 K magnetic field (H) dependence of σ_{xy} at the same V_g as in panels (a, b). The inset to panel (c) is a zoomed-in view of the solid green and blue data, at 1.1 and 1.3 V, showing the vanishing of the anomalous Hall effect in the BM phase. For accuracy, in all parts of this figure, data after gating to the BM phase were treated using the reduced thickness determined from Figure 3.

induce a second P → BM transformation. The open circles here label the minimum V_g for each loop. The data reveal a new phenomenon, where the threshold V_g at which I_{SD} begins to decrease on the second cycle progressively decreases with the minimum (negative) V_g applied during the first cycle. By the time the blue curve is reached, for example (minimum V_g = −3.5 V), the threshold V_g on the second cycle has shifted to negative voltage, indicating substantial reduction from P to BM even at V_g = 0. By a minimum applied V_g of −4.0 V (purple), the second-cycle P → BM transformation appears to be near-complete by V_g = 0. It must be emphasized that such behavior corresponds to a loss of nonvolatile retention of the P (ON) and BM (OFF) states at V_g = 0, which would be undesirable for some applications. Figure 5(h) shows that the second-cycle P → BM transformations are again marked by two peaks in the logarithmic derivative (as in Figure 4(b)), the positions of which are plotted vs minimum (negative) V_g on the first cycle in Figure 5(i). The threshold voltages are approximately constant (and positive), down to −2 V. At lower minimum V_g, however, they decrease, switching sign below ∼ −3.5 V. To avoid this inversion in threshold voltage on the second cycle, the minimum (negative) V_g applied should thus be above ∼ −3.5 V. In totality, the analyses of minor loops in Figure 5 thus quantitatively establish the optimal operating range of ion-gel-gated LSCO for the first time, at approximately −3.5 V < V_g < 3.0 V. This range ensures large enough maximum V_g to obtain high ON/OFF ratio at workable recovery ratio, while the minimum V_g is large enough to avoid the threshold voltage inversion on the second cycle.

At the highest level, the above analysis of minor $I_{SD}(V_g)$ loops simply establishes a general finding that is highly analogous to more extensively studied electrochemical devices such as Li-ion batteries.[79] Specifically, limits on voltages must be adhered to for maximal cyclability,[80] in order to avoid overoxidation and overreduction of the electrodes, in this case specifically LSCO. Deeper understanding of the specifics of the origins of the overoxidation and overreduction phenomena in LSCO electrochemical transistors is more challenging and requires separation of effects in the LSCO, the electrolyte, and their interface. With respect to the limit on the maximum (positive) V_g that can be applied (Figure 5(a−c)), we believe that the LSCO itself is not the limiting factor. Multiple observations, including optical inspection of failed devices and lower recovery ratios in I_{SD} compared to ρ (discussed above with Figures 2(a) and 4(a) and returned to with Figure 6(a)), in fact indicate that device factors, particularly contact degradation,[30] are the central issue (see also Supporting Information Section C, Figure S4). Further work could thus realize substantial improvements through better device design, for example, with regard to the overlap of contact regions and the electrolyte. With respect to the limit on the minimum (negative) V_g that can be applied, conversely, we believe that the LSCO may be the limiting factor. As shown in Figure 5(g), application of negative V_g below this limit does not prevent reduction to BM on the second cycle, indicating that the devices continue to function. Large negative V_g instead likely overoxidizes x = 0.5 LSCO to the point that the mean Co valence reaches the limits of stability of a 10-unit-cell film at ambient conditions,[18,67] making V_O formation spontaneous as the V_g sweep direction is reversed, as in the blue and purple curves in Figure 5(g). This is the same phenomenon detected in earlier work through cruder voltage-step measurements.[18,67] Another possible cause, however, could be electrochemical degradation of anions in the ion gel ($TFSI^-$ in this case), which may break down at lower V_g magnitudes than the cations (EMI^+).[81,82] This would result in a shift of the charge neutral

https://doi.org/10.1021/acsami.4c01336
ACS Appl. Mater. Interfaces 2024, 16, 19184−19197

point to lower (i.e., negative) V_g; further study is needed to deconvolute these effects.

With the optimal parameters for V_g cycling established, Figure 6 focuses on magnetotransport and magnetic properties of ion-gel-gated LAO/LSCO(10-unit-cell) films around the P → BM → P cycle. The inset to Figure 6(a) first shows a typical 300 K $I_{SD}(V_g)$ loop, from 0 V → 2.5 V → −3.5 V, i.e., within the determined optimal range. The colored points on the loop indicate voltages at which the loop was paused and the device cooled, to perform $\rho(T)$ and Hall effect measurements, before rewarming and continuing the V_g sweep. As shown in the main panel of Figure 6(a), the initial (V_g = 0) state of these LAO/LSCO(10-unit-cell) films corresponds to state-of-the-art metallic $\rho(T)$ (black line) with a residual resistivity ratio of 2.0.[67,68] The inflection point at ∼165 K marks T_C[67,68,70] (see Supporting Information Section C, Figure S5), which is comparable to the best reports at this thickness.[67−70] As V_g is increased to 0.9 V (yellow line; the inset and panel (a) are color-coordinated), weakly metallic behavior persists, but with increased residual resistivity, consistent with increased δ in the P phase. This situation changes at 1.1 V (green line) where $\rho(T)$ becomes insulating and $\rho(T \to 0)$ exceeds the quantum resistance multiplied by thickness, $(h/e^2)t$. This indicates a metal−insulator transition, very close to the point at which the sharp decrease in I_{SD} occurs in the inset, and to the point at which the first BM forms (from Figures 2−5). At larger V_g, progressively more insulating behavior evolves, eventually reaching the brown (2.5 V) line in Figure 6(a), where the 300 K ρ is 1.3×10^4 times higher than the initial state, and ρ rapidly increases on cooling; this corresponds to nominally phase-pure BM. More details on the nature of the transport in this state are provided in Supporting Information Section C, Figure S6. At intermediate V_g, the forms of $\rho(T)$ are somewhat unusual due to P-BM coexistence and thus inhomogeneous transport.[18,23] The dashed lines in Figure 6(a) then show the evolution in $\rho(T)$ on gating back to the P state. Close-to-metallic transport first emerges at −3.0 V (light blue dashed line), followed at −3.5 V (green dashed line) by metallic behavior. The latter is unambiguous, from finite $\rho(T \to 0)$, $\rho < (h/e^2)t$, and the substantial regime of positive $d\rho/dT$. Our optimal V_g cycle thus enables nonvolatile metal → insulator → metal cycling around the P → BM → P transformation. Consistent with one of the main messages from above, however (Figures 2−5), the recovery of the metallic P state is imperfect. The V_g = −3.5 V curve in Figure 6(a) is in fact similar to the V_g = 0.9 V curve, the 300 K ρ being 1.8 times larger than in the initial state. This is due to the combined effects of diminished structural perfection in the recovered P state (Figures 2(g) and 3(a,d)), slightly higher δ (Figure 3(g) and Supporting Information Section C, Figure S7), and higher surface roughness (Figures 2(g) and 3(a,d,f)). Again, the recovery is better in terms of ρ than I_{SD}, indicating contact degradation (see also Supporting Information Section C, Figure S4).

Notably, the V_g = −3.5 V curve in Figure 6(a) displays an inflection point at ∼145 K (Supporting Information Section C, Figure S5), strongly suggesting a well-defined T_C (∼20 K below the initial value),[67,68,70] which would indicate true F → non-F → F cycling. This was probed further through anomalous Hall effect measurements, which offer distinct advantages over (signal-limited) magnetometry measurements in such thin films.[67,68] Figure 6(b) therefore shows the T-dependence of the remanent transverse (Hall) conductivity, $\sigma_{xy} = [\rho_{xy}(T, 50\ \text{Oe}) - \rho_{xy}(T, -50\ \text{Oe})]/2[\rho_{xx}(T, 0)]^2$. The V_g = 0 behavior is characteristic of LSCO,[67,68,83] exhibiting a sharp turn on in σ_{xy} at $T_C \approx 168$ K (in reasonable agreement with our estimate from $\rho(T)$ and expectations at this thickness;[67−69] see Supporting Information Section C, Figure S8), and a broad maximum at intermediate T. This is characteristic of the anomalous Hall effect in x = 0.5 LSCO.[83] As V_g is increased, σ_{xy} progressively decreases in amplitude down to 0.9 V (yellow solid line). By 1.1 V (green solid line), coincident with the metal−insulator transition in Figure 6(a), σ_{xy} practically vanishes, evidencing only a weak magnetic transition at ∼150 K. This is consistent with prior work on LSCO bulk crystals[84] and epitaxial films,[69,85] which lose metallicity near $T_C \approx 150$ K, effective dopings beneath this inducing glassy, phase-separated magnetism.[86] As V_g is reversed in Figure 6(b), critically, a F-like $\sigma_{xy}(T)$ re-emerges, the −3.5 V case (green dashed line, $T_C \approx 152$ K, see Supporting Information Figure S8) coinciding closely with the 0.9 V case (yellow solid line), as for $\rho(T)$ in Figure 6(a). Our optimal V_g cycle thus enables nonvolatile F → non-F → F cycling in addition to metal → insulator → metal cycling. We emphasize that while the non-F BM phase of bulk $SrCoO_{2.5}$ is known to be AF with a high T_N of 540 K,[50] AF order in electrochemically reduced $SrCoO_{2.5}$ films has not been directly verified. In x = 0.5 LSCO, the existence or otherwise of AF order is not established in bulk, let alone gated films. Further work to address this issue is therefore clearly needed, and we thus refer to BM LSCO films here simply as "non-F".

Finally, Figure 6(c) provides additional insight into V_g cycling of magnetic properties by plotting 50-K σ_{xy} vs applied perpendicular magnetic field (H) hysteresis loops at various V_g. The behavior is remarkably simple, the square, wide, hysteresis loops simply dropping in amplitude as V_g increases from 0 to 0.9 V (LSCO films under compressive stress are known to have substantial perpendicular magnetic anisotropy[69]). At V_g = 1.1 V, coincident with the metal−insulator transition in Figure 6(a), and consistent with $\sigma_{xy}(T)$ in Figure 6(b), F behavior in $\sigma_{xy}(H)$ almost vanishes. As emphasized in the close-up in the inset to Figure 6(c), the anomalous Hall effect truly disappears by 1.3 V. Consistent with Figure 6(a,b), reversing V_g to −3.5 V then recovers the F state (green dashed line), albeit with diminished maximum σ_{xy} relative to the as-deposited P state. As for Figure 6(a,b), the incomplete recovery of as-deposited properties is due to the effects of diminished structural perfection, higher δ, and higher roughness in the recovered P state.

CONCLUSIONS

In summary, we have presented the first full study of hysteresis and reversibility across the voltage-induced P ↔ BM topotactic phase transformation in electrochemically gated perovskite cobaltite thin films. Gate-voltage hysteresis loops around the entire P → BM → P cycle reveal a wealth of new mechanistic understanding, particularly in tandem with quantitative operando SXRD. Examples include asymmetric hysteresis due to differing oxygen diffusion characteristics in the P and BM phases, nonmonotonic transformation rates due to the first-order nature of the transformation, and limits on first-cycle recovery due to diminished structural coherence, oxygen content, and surface perfection. Extensive minor hysteresis loop studies were then shown to provide yet deeper insight, enabling the first rational and quantitative design of an optimal gate-voltage cycle in such devices. This cycle was then used to

https://doi.org/10.1021/acsami.4c01336
ACS Appl. Mater. Interfaces 2024, 16, 19184−19197

realize state-of-the-art voltage control of transport and magnetic properties, encompassing >10^5 room-temperature ON/OFF ratios, high recovery, and metal → insulator → metal and ferromagnet → nonferromagnet → ferromagnet cycling, all with high room-temperature stability and nonvolatility. This was achieved in ultrathin (10-unit-cell) ion-gel-gated $La_{0.5}Sr_{0.5}CoO_{3-\delta}$ thin films, setting the stage for future assessment of the ultimate limits on the switching speed and durability of such redox-based electrochemical transistors.

■ METHODS

10-unit-cell-thick P LSCO films were deposited from ceramic targets onto single-crystal LAO(001) substrates by high-pressure-oxygen sputter deposition. High-quality, extensively characterized LSCO films have been reported previously via this method.[18,23,29,67−70] In brief, typically 5 × 5 mm^2 LAO substrates (MTI Corp.) were preannealed for 15 min in ∼1 Torr of flowing O_2 at 900 °C. Previously optimized deposition conditions were employed,[18,23,29,67−70] involving 600 °C substrate temperature, 1.5 Torr O_2 pressure, and 55−65 W sputtering power, resulting in 15−20 Å min^{-1} growth rates (calibrated from XRD Laue fringes). Post deposition, films were cooled in 600 Torr of O_2 to minimize δ in the P phase; based on resistivity,[68] an as-grown $\delta \approx 0.14$ was estimated. Side-gate electrolyte transistors (Figure 1(c)) were then fabricated from LAO/LSCO films using a series of steel masks, Ar ion milling, sputtering of Pt film and gate electrodes, and ion-gel lamination.[18,23,29,67,68,72] Ion gels were first spin-coated onto sacrificial glass wafers from a 1:4:8 (by weight) solution of polymer (P(VDF-HFP))/ionic liquid (EMIM-TFSI)/solvent (acetone),[18,23,29,67,68,72] followed by drying in vacuum at 70 °C for 1 day. Here, VDF is vinylidene fluoride, HFP is hexafluoropropylene, EMIM is 1-ethyl-3-methylimidazolium, and TFSI is bis-(trifluoromethylsulfonyl)imide. Gels were then applied to LSCO devices using "cut and stick" methods.[1,87] Devices with 1.0 × 1.0 mm^2 channels were used for all measurements except operando SXRD, which employed 4.0 × 3.5 mm^2 channels (Figure 1(c)), which necessitated the use of larger, 10 × 10 mm^2 LAO substrates.

Electrolyte gating was typically performed at 300 K in vacuum (<10^{-5} Torr), as in many prior works. V_g and I_g were applied and measured with a Keithley 2400 source-measure unit, and V_g was swept at 1 mV s^{-1} unless otherwise specified. I_{SD} and the four-terminal van der Pauw sheet resistance and ρ were then measured with a Keithley 2400 source-measure unit and a Keithley 2002 multimeter, using a source−drain voltage alternating (for offset compensation) between ±0.1 V. Operando T- and H-dependent transport measurements were made in a Quantum Design Physical Property Measurement System from 10 to 300 K in fields up to 90 kOe. After sweeping at 1 mV s^{-1} to a chosen V_g (at 300 K), devices were then cooled to 10 at 3 K min^{-1}, and $\rho(T)$ measured on warming at 1 K min^{-1}. After recooling, Hall resistance measurements were made in ±90 kOe to determine $\sigma_{xy}(T)$, accompanied by measurement of $\sigma_{xy}(H)$ loops at 50 K. Rewarming (at 1 K min^{-1}) to 300 K was then performed before sweeping to the next V_g. Keithley-based DC measurements were again utilized, with careful choice of excitation currents to avoid self-heating and nonohmicity.

Operando SXRD during ion-gel gating was done at beamline 12-ID-D of the Advanced Photon Source, Argonne National Laboratory, using a five-circle Huber goniometer. Twenty-two keV incident X-rays (∼0.59 Å wavelength) with a lateral beam spot size ∼200 μm were illuminated on the LSCO channel area, and scattered X-rays were collected by a Pilatus II 100 K 2D pixeled area detector. While operando V_g sweeps were performed at 300 K (under pure N_2), diffraction data were taken at 150 K (using a liquid-N_2-flow cryocooler) to minimize beam damage; each scan took ∼30 min. To further mitigate potential beam damage, each scan was acquired on a fresh film spot, shifted by ∼500 μm from the prior one. Background subtraction employed a Matlab routine specific to the beamline. As noted in the main text, the structural refinement employed is described in full in the Supporting Information. Briefly, this involves a one-dimensional substrate−interface-film model and a newly developed constrained-phase-retrieval algorithm. The model describes the one-dimensional projected (averaged) electron density along the in-plane directions as a function of depth for the film and substrate. The electron density of each atomic layer and the corresponding positions are determined by minimizing the mean-square error between the model-predicted and observed intensities.

■ ASSOCIATED CONTENT

Supporting Information

The Supporting Information is available free of charge at https://pubs.acs.org/doi/10.1021/acsami.4c01336.

SXRD data and the constrained-phase-retrieval algorithm; additional structural characterization from SXRD data and analysis; and additional (magneto)transport data and analysis (PDF)

■ AUTHOR INFORMATION

Corresponding Author

Chris Leighton − *Department of Chemical Engineering and Materials Science, University of Minnesota, Minneapolis, Minnesota 55455, United States;* orcid.org/0000-0003-2492-0816; Email: leighton@umn.edu

Authors

William M. Postiglione − *Department of Chemical Engineering and Materials Science, University of Minnesota, Minneapolis, Minnesota 55455, United States;* orcid.org/0000-0002-5301-863X

Guichuan Yu − *Minnesota Supercomputing Institute, University of Minnesota, Minneapolis, Minnesota 55455, United States; Characterization Facility, University of Minnesota, Minneapolis, Minnesota 55455, United States*

Vipul Chaturvedi − *Department of Chemical Engineering and Materials Science, University of Minnesota, Minneapolis, Minnesota 55455, United States;* orcid.org/0000-0001-6121-4756

Hua Zhou − *Advanced Photon Source, Argonne National Laboratory, Lemont, Illinois 60439, United States;* orcid.org/0000-0001-9642-8674

Kei Heltemes − *Department of Chemical Engineering and Materials Science, University of Minnesota, Minneapolis, Minnesota 55455, United States*

Andrew Jacobson − *Department of Chemical Engineering and Materials Science, University of Minnesota, Minneapolis, Minnesota 55455, United States*

Martin Greven − *School of Physics and Astronomy, University of Minnesota, Minneapolis, Minnesota 55455, United States*

Complete contact information is available at: https://pubs.acs.org/10.1021/acsami.4c01336

Notes

The authors declare no competing financial interest.

■ ACKNOWLEDGMENTS

This work was supported primarily by the National Science Foundation through the University of Minnesota MRSEC under Award Number DMR-2011401. Parts of this work were performed in the Characterization Facility, UMN, which receives partial support from NSF through the MRSEC and NNCI programs. Portions of this work were also conducted in the Minnesota Nano Center, which is supported by NSF through the National Nano Coordinated Infrastructure

(NNCI) under ECCS-2025124. This work also used resources of the Advanced Photon Source, a DOE Office of Science User Facility operated by the Argonne National Laboratory under Contract No. DE-AC02-06CH11357. The Minnesota Supercomputing Institute (MSI) at the University of Minnesota provided resources that contributed to the X-ray data analysis reported within this paper.

REFERENCES

(1) Kim, S. H.; Hong, K.; Xie, W.; Lee, K. H.; Zhang, S.; Lodge, T. P.; Frisbie, C. D. Electrolyte-Gated Transistors for Organic and Printed Electronics. *Adv. Mater.* **2013**, *25*, 1822−1846.

(2) Leighton, C. Electrolyte-Based Ionic Control of Functional Oxides. *Nat. Mater.* **2019**, *18*, 13−18.

(3) Bisri, S. Z.; Shimizu, S.; Nakano, M.; Iwasa, Y. Endeavor of Iontronics: From Fundamentals to Applications of Ion-Controlled Electronics. *Adv. Mater.* **2017**, *29*, No. 1607054.

(4) Leighton, C.; Birol, T.; Walter, J. What Controls Electrostatic vs Electrochemical Response in Electrolyte-Gated Materials? A Perspective on Critical Materials Factors. *APL Mater.* **2022**, *10*, No. 040901.

(5) Guan, Y.; Han, H.; Li, F.; Li, G.; Parkin, S. S. P. Ionic Gating for Tuning Electronic and Magnetic Properties. *Annu. Rev. Mater. Res.* **2023**, *53*, 25−51.

(6) Navarro-Senent, C.; Quintana, A.; Menéndez, E.; Pellicer, E.; Sort, J. Electrolyte-Gated Magnetoelectric Actuation: Phenomenology, Materials, Mechanisms, and Prospective Applications. *APL Mater.* **2019**, *7*, No. 030701.

(7) Nichterwitz, M.; Honnali, S.; Kutuzau, M.; Guo, S.; Zehner, J.; Nielsch, K.; Leistner, K. Advances in Magneto-Ionic Materials and Perspectives for Their Application. *APL Mater.* **2021**, *9*, No. 030903.

(8) Jeong, J.; Aetukuri, N.; Graf, T.; Schladt, T. D.; Samant, M. G.; Parkin, S. S. P. Suppression of Metal-Insulator Transition in VO_2 by Electric Field-Induced Oxygen Vacancy Formation. *Science* **2013**, *339*, 1402−1405.

(9) Bi, C.; Liu, Y.; Newhouse-Illige, T.; Xu, M.; Rosales, M.; Freeland, J. W.; Mryasov, O.; Zhang, S.; te Velthuis, S. G. E.; Wang, W. G. Reversible Control of Co Magnetism by Voltage-Induced Oxidation. *Phys. Rev. Lett.* **2014**, *113*, No. 267202.

(10) Bauer, U.; Yao, L.; Tan, A. J.; Agrawal, P.; Emori, S.; Tuller, H. L.; Van Dijken, S.; Beach, G. S. D. Magneto-Ionic Control of Interfacial Magnetism. *Nat. Mater.* **2015**, *14*, 174−181.

(11) Lu, Q.; Yildiz, B. Voltage-Controlled Topotactic Phase Transition in Thin-Film $SrCoO_x$ Monitored by In Situ X-Ray Diffraction. *Nano Lett.* **2016**, *16*, 1186−1193.

(12) Lu, Q.; Chen, Y.; Bluhm, H.; Yildiz, B. Electronic Structure Evolution of $SrCoO_x$ During Electrochemically Driven Phase Transition Probed by *In Situ* X-Ray Spectroscopy. *J. Phys. Chem. C* **2016**, *120*, 24148−24157.

(13) Lu, N.; Zhang, P.; Zhang, Q.; Qiao, R.; He, Q.; Li, H.-B.; Wang, Y.; Guo, J.; Zhang, D.; Duan, Z.; Li, Z.; Wang, M.; Yang, S.; Yan, M.; Arenholz, E.; Zhou, S.; Yang, W.; Gu, L.; Nan, C.-W.; Wu, J.; et al. Electric-Field Control of Tri-State Phase Transformation with a Selective Dual-Ion Switch. *Nature* **2017**, *546*, 124−128.

(14) Cui, B.; Werner, P.; Ma, T.; Zhong, X.; Wang, Z.; Taylor, J. M.; Zhuang, Y.; Parkin, S. S. P. Direct Imaging of Structural Changes Induced by Ionic Liquid Gating Leading to Engineered Three-Dimensional Meso-Structures. *Nat. Commun.* **2018**, *9*, No. 3055.

(15) Saleem, M. S.; Cui, B.; Song, C.; Sun, Y.; Gu, Y.; Zhang, R.; Fayaz, M. U.; Zhou, X.; Werner, P.; Parkin, S. S. P.; Pan, F. Electric Field Control of Phase Transition and Tunable Resistive Switching in $SrFeO_{2.5}$. *ACS Appl. Mater. Interfaces* **2019**, *11*, 6581−6588.

(16) Hu, S.; Han, W.; Hu, S.; Seidel, J.; Wang, J.; Wu, R.; Wang, J.; Zhao, J.; Xu, Z.; Ye, M.; Chen, L. Voltage-Controlled Oxygen Non-Stoichiometry in $SrCoO_{3-\delta}$ Thin Films. *Chem. Mater.* **2019**, *31*, 6117−6123.

(17) Yi, D.; Wang, Y.; van 't Erve, O. M. J.; Xu, L.; Yuan, H.; Veit, M. J.; Balakrishnan, P. P.; Choi, Y.; N'Diaye, A. T.; Shafer, P.; Arenholz, E.; Grutter, A.; Xu, H.; Yu, P.; Jonker, B. T.; Suzuki, Y. Emergent Electric Field Control of Phase Transformation in Oxide Superlattices. *Nat. Commun.* **2020**, *11*, No. 902.

(18) Chaturvedi, V.; Postiglione, W. M.; Chakraborty, R. D.; Yu, B.; Tabiś, W.; Hameed, S.; Biniskos, N.; Jacobson, A.; Zhang, Z.; Zhou, H.; Greven, M.; Ferry, V. E.; Leighton, C. Doping- and Strain-Dependent Electrolyte-Gate-Induced Perovskite to Brownmillerite Transformation in Epitaxial $La_{1-x}Sr_xCoO_{3-\delta}$ Films. *ACS Appl. Mater. Interfaces* **2021**, *13*, 51205−51217.

(19) Ning, S.; Zhang, Q.; Occhialini, C.; Comin, R.; Zhong, X.; Ross, C. A. Voltage Control of Magnetism Above Room Temperature in Epitaxial $SrCo_{1-x}Fe_xO_{3-\delta}$. *ACS Nano* **2020**, *14*, 8949−8957.

(20) Wang, D.; Meng, L.; Wei, L.; Shi, P.; Chen, Y.; Yan, S.; Tian, Y.; Liu, G.; Mei, L. Reversible Phase Switching Between Antiferromagnetic $SrCoO_{2.5}$ and Ferromagnetic $SrCoO_{3-\delta}$ by a Flexible Solid-State Electrolyte Gate. *J. Magn. Magn. Mater.* **2020**, *496*, No. 165926.

(21) Han, H.; Sharma, A.; Meyerheim, H. L.; Yoon, J.; Deniz, H.; Jeon, K.-R.; Sharma, A. K.; Mohseni, K.; Guillemard, C.; Valvidares, M.; Gargiani, P.; Parkin, S. S. P. Control of Oxygen Vacancy Ordering in Brownmillerite Thin Films via Ionic Liquid Gating. *ACS Nano* **2022**, *16*, 6206−6214.

(22) Yin, Z.; Wang, J.; Wang, J.; Li, J.; Zhou, H.; Zhang, C.; Zhang, H.; Zhang, J.; Shen, F.; Hao, J.; Yu, Z.; Gao, Y.; Wang, Y.; Chen, Y.; Sun, J.-R.; Bai, X.; Wang, J.-T.; Hu, F.; Zhao, T.-Y.; Shen, B. Compressive-Strain-Facilitated Fast Oxygen Migration with Reversible Topotactic Transformation in La $_{0.5}Sr_{0.5}CoO_x$ via All-Solid-State Electrolyte Gating. *ACS Nano* **2022**, *16*, 14632−14643.

(23) Zhang, Y.; Postiglione, W. M.; Xie, R.; Zhang, C.; Zhou, H.; Chaturvedi, V.; Heltemes, K.; Zhou, H.; Feng, T.; Leighton, C.; Wang, X. Wide-Range Continuous Tuning of the Thermal Conductivity of $La_{0.5}Sr_{0.5}CoO_{3-\delta}$ Films via Room-Temperature Ion-Gel Gating. *Nat. Commun.* **2023**, *14*, No. 2626.

(24) Huang, H.-Y.; Ge, C.; Zhang, Q.-H.; Liu, C.-X.; Du, J.-Y.; Li, J.-K.; Wang, C.; Gu, L.; Yang, G.-Z.; Jin, K.-J. Electrolyte-Gated Synaptic Transistor with Oxygen Ions. *Adv. Funct. Mater.* **2019**, *29*, No. 1902702.

(25) Lu, Q.; Huberman, S.; Zhang, H.; Song, Q.; Wang, J.; Vardar, G.; Hunt, A.; Waluyo, I.; Chen, G.; Yildiz, B. Bi-Directional Tuning of Thermal Transport in $SrCoO_x$ with Electrochemically Induced Phase Transitions. *Nat. Mater.* **2020**, *19*, 655−662.

(26) Miao, T.; Cui, B.; Huang, C.; Wang, D.; Liu, L.; Liu, W.; Li, Y.; Chu, R.; Ren, X.; Liu, L.; Cheng, B.; Zhou, G.; Qin, H.; Xing, G.; Hu, J. Gate-Tunable Anisotropic Oxygen Ion Migration in $SrCoO_x$: Toward Emerging Oxide-Based Artificial Synapses. *Adv. Intell. Syst.* **2023**, *5*, No. 2200287.

(27) Zhuang, Y.; Cui, B.; Yang, H.; Gao, F.; Parkin, S. S. P. Ionic Liquid Gate-Induced Modifications of Step Edges at $SrCoO_{2.5}$ Surfaces. *ACS Nano* **2020**, *14*, 8562−8569.

(28) Sood, A.; Poletayev, A. D.; Cogswell, D. A.; Csernica, P. M.; Mefford, J. T.; Fraggedakis, D.; Toney, M. F.; Lindenberg, A. M.; Bazant, M. Z.; Chueh, W. C. Electrochemical Ion Insertion from the Atomic to the Device Scale. *Nat. Rev. Mater.* **2021**, *6*, 847−867.

(29) Chakraborty, R. D.; Postiglione, W. M.; Ghosh, S.; Mkhoyan, K. A.; Leighton, C.; Ferry, V. E. Optical Properties of Electrochemically Gated $La_{1-x}Sr_xCoO_{3-\delta}$ as a Topotactic Phase-Change Material. *Adv. Opt. Mater.* **2023**, *11*, No. 2300098.

(30) Lefler, B. M.; Postiglione, W. M.; Leighton, C.; May, S. J. Voltage Control of Patterned Metal/Insulator Properties in Oxide/Oxyfluoride Lateral Perovskite Heterostructures via Ion Gel Gating. *Adv. Funct. Mater.* **2022**, *32*, No. 2208434.

(31) Yang, Q.; Lee, J.; Jeen, H.; Cho, H. J.; Ohta, H. Solid-State Electrochemical Protonation of $SrCoO_{2.5}$ into $H_xSrCoO_{2.5}$ (x = 1, 1.5, and 2). *ACS Appl. Electron. Mater.* **2021**, *3*, 3296−3300.

(32) Gilbert, D. A.; Grutter, A. J.; Murray, P. D.; Chopdekar, R. V.; Kane, A. M.; Ionin, A. L.; Lee, M. S.; Spurgeon, S. R.; Kirby, B. J.; Maranville, B. B.; N'Diaye, A. T.; Mehta, A.; Arenholz, E.; Liu, K.; Takamura, Y.; Borchers, J. A. Ionic Tuning of Cobaltites at the Nanoscale. *Phys. Rev. Mater.* **2018**, *2*, No. 104402.

https://doi.org/10.1021/acsami.4c01336
ACS Appl. Mater. Interfaces 2024, 16, 19184−19197

(33) Rippy, G.; Trinh, L.; Kane, A. M.; Ionin, A. L.; Lee, M. S.; Chopdekar, R. V.; Christiansen-Salameh, J. M.; Gilbert, D. A.; Grutter, A. J.; Murray, P. D.; Holt, M. V.; Cai, Z.; Liu, K.; Takamura, Y.; Kukreja, R. X-Ray Nanodiffraction Studies of Ionically Controlled Nanoscale Phase Separation in Cobaltites. *Phys. Rev. Mater.* **2019**, *3*, No. 082001.

(34) Wang, M.; Shen, S.; Ni, J.; Lu, N.; Li, Z.; Li, H.-B.; Yang, S.; Chen, T.; Guo, J.; Wang, Y.; Xiang, H.; Yu, P. Electric-Field-Controlled Phase Transformation in WO_3 Thin Films through Hydrogen Evolution. *Adv. Mater.* **2017**, *29*, No. 1703628.

(35) Tan, A. J.; Huang, M.; Avci, C. O.; Büttner, F.; Mann, M.; Hu, W.; Mazzoli, C.; Wilkins, S.; Tuller, H. L.; Beach, G. S. D. Magneto-Ionic Control of Magnetism Using a Solid-State Proton Pump. *Nat. Mater.* **2019**, *18*, 35−41.

(36) Yu, Y.; Yang, F.; Lu, X. F.; Yan, Y. J.; Cho, Y.-H.; Ma, L.; Niu, X.; Kim, S.; Son, Y.-W.; Feng, D.; Li, S.; Cheong, S.-W.; Chen, X. H.; Zhang, Y. Gate-Tunable Phase Transitions in Thin Flakes of 1T-TaS_2. *Nat. Nanotechnol.* **2015**, *10*, 270−276.

(37) Ameziane, M.; Rosenkamp, R.; Flajšman, L.; van Dijken, S.; Mansell, R. Electric Field Control of RKKY Coupling through Solid-State Ionics. *Appl. Phys. Lett.* **2023**, *122*, No. 232401.

(38) de Rojas, J.; Quintana, A.; Lopeandía, A.; Salguero, J.; Muñiz, B.; Ibrahim, F.; Chshiev, M.; Nicolenco, A.; Liedke, M. O.; Butterling, M.; Wagner, A.; Sireus, V.; Abad, L.; Jensen, C. J.; Liu, K.; Nogués, J.; Costa-Krämer, J. L.; Menéndez, E.; Sort, J. Voltage-Driven Motion of Nitrogen Ions: A New Paradigm for Magneto-Ionics. *Nat. Commun.* **2020**, *11*, No. 5871.

(39) de Rojas, J.; Quintana, A.; Rius, G.; Stefani, C.; Domingo, N.; Costa-Krämer, J. L.; Menéndez, E.; Sort, J. Voltage Control of Magnetism with Magneto-Ionic Approaches: Beyond Voltage-Driven Oxygen Ion Migration. *Appl. Phys. Lett.* **2022**, *120*, No. 070501.

(40) Namba, M.; Takatsu, H.; Li, H.-B.; Murayama, K.; Terada, R.; Yang, Q.; Terashima, T.; Ohta, H.; Kageyama, H. Pure Fluorine Intercalation into Brownmillerite Oxide Thin Films by Using Ionic Liquid Gating. *Chem. Mater.* **2024**, *36*, 2076−2084.

(41) Hoffmann, A.; Ramanathan, S.; Grollier, J.; Kent, A. D.; Rozenberg, M. J.; Schuller, I. K.; Shpyrko, O. G.; Dynes, R. C.; Fainman, Y.; Frano, A.; Fullerton, E. E.; Galli, G.; Lomakin, V.; Ong, S. P.; Petford-Long, A. K.; Schuller, J. A.; Stiles, M. D.; Takamura, Y.; Zhu, Y. Quantum Materials for Energy-Efficient Neuromorphic Computing: Opportunities and Challenges. *APL Mater.* **2022**, *10*, No. 070904.

(42) Wexler, R. B.; Gautam, G. S.; Stechel, E. B.; Carter, E. A. Factors Governing Oxygen Vacancy Formation in Oxide Perovskites. *J. Am. Chem. Soc.* **2021**, *143*, 13212−13227.

(43) Tahini, H. A.; Tan, X.; Schwingenschlögl, U.; Smith, S. C. Formation and Migration of Oxygen Vacancies in $SrCoO_3$ and Their Effect on Oxygen Evolution Reactions. *ACS Catal.* **2016**, *6*, 5565−5570.

(44) Zhang, S.; Galli, G. Understanding the Metal-to-Insulator Transition in $La_{1-x}Sr_xCoO_{3-\delta}$ and Its Applications for Neuromorphic Computing. *NPJ Comput. Mater.* **2020**, *6*, 170.

(45) Zhang, S.; Vo, H.; Galli, G. Predicting the Onset of Metal−Insulator Transitions in Transition Metal Oxides—A First Step in Designing Neuromorphic Devices. *Chem. Mater.* **2021**, *33*, 3187−3195.

(46) Takeda, Y.; Kanno, R.; Takada, T.; Yamamoto, O.; Takano, M.; Bando, Y. Phase Relation and Oxygen-Non-Stoichiometry of Perovskite-Like Compound $SrCoO_x$ ($2.29 < x > 2.80$). *Z. Anorg. Allg. Chem.* **1986**, *540*, 259−270.

(47) Nemudry, A.; Goldberg, E. L.; Aguirre, M.; Alario-Franco, M. Á. Electrochemical Topotactic Oxidation of Nonstoichiometric Perovskites at Ambient Temperature. *Solid State Sci.* **2002**, *4*, 677−690.

(48) Mefford, J. T.; Rong, X.; Abakumov, A. M.; Hardin, W. G.; Dai, S.; Kolpak, A. M.; Johnston, K. P.; Stevenson, K. J. Water Electrolysis on $La_{1-x}Sr_xCoO_{3-\delta}$ Perovskite Electrocatalysts. *Nat. Commun.* **2016**, *7*, No. 11053.

(49) Long, Y.; Kaneko, Y.; Ishiwata, S.; Taguchi, Y.; Tokura, Y. Synthesis of Cubic $SrCoO_3$ Single Crystal and Its Anisotropic Magnetic and Transport Properties. *J. Phys.: Condens. Matter* **2011**, *23*, No. 245601.

(50) Muñoz, A.; de la Calle, C.; Alonso, J. A.; Botta, P. M.; Pardo, V.; Baldomir, D.; Rivas, J. Crystallographic and Magnetic Structure of $SrCoO_{2.5}$ Brownmillerite: Neutron Study Coupled with Band-Structure Calculations. *Phys. Rev. B* **2008**, *78*, No. 054404.

(51) Nemudry, A.; Rudolf, P.; Schöllhorn, R. Topotactic Electrochemical Redox Reactions of the Defect Perovskite $SrCoO_{2.5+x}$. *Chem. Mater.* **1996**, *8*, 2232−2238.

(52) Le Toquin, R.; Paulus, W.; Cousson, A.; Prestipino, C.; Lamberti, C. Time-Resolved In Situ Studies of Oxygen Intercalation into $SrCoO_{2.5}$, Performed by Neutron Diffraction and X-Ray Absorption Spectroscopy. *J. Am. Chem. Soc.* **2006**, *128*, 13161−13174.

(53) Klie, R. F.; Ito, Y.; Stemmer, S.; Browning, N. D. Observation of Oxygen Vacancy Ordering and Segregation in Perovskite Oxides. *Ultramicroscopy* **2001**, *86*, 289−302.

(54) Ito, Y.; Klie, R. F.; Browning, N. D.; Mazanec, T. J. Atomic Resolution Analysis of the Defect Chemistry and Microdomain Structure of Brownmillerite-Type Strontium Cobaltite. *J. Am. Ceram. Soc.* **2002**, *85*, 969−976.

(55) Jeen, H.; Choi, W. S.; Biegalski, M. D.; Folkman, C. M.; Tung, I.-C.; Fong, D. D.; Freeland, J. W.; Shin, D.; Ohta, H.; Chisholm, M. F.; Lee, H. N. Reversible Redox Reactions in an Epitaxially Stabilized $SrCoO_x$ Oxygen Sponge. *Nat. Mater.* **2013**, *12*, 1057−1063.

(56) Jeen, H.; Choi, W. S.; Freeland, J. W.; Ohta, H.; Jung, C. U.; Lee, H. N. Topotactic Phase Transformation of the Brownmillerite $SrCoO_{2.5}$ to the Perovskite $SrCoO_{3-\delta}$. *Adv. Mater.* **2013**, *25*, 3651−3656.

(57) Tambunan, O. T.; Parwanta, K. J.; Acharya, S. K.; Lee, B. W.; Jung, C. U.; Kim, Y. S.; Park, B. H.; Jeong, H.; Park, J.-Y.; Cho, M. R.; Park, Y. D.; Choi, W. S.; Kim, D.-W.; Jin, H.; Lee, S.; Song, S. J.; Kang, S.-J.; Kim, M.; Hwang, C. S. Resistance Switching in Epitaxial $SrCoO_x$ Thin Films. *Appl. Phys. Lett.* **2014**, *105*, No. 063507.

(58) Acharya, S. K.; Nallagatla, R. V.; Togibasa, O.; Lee, B. W.; Liu, C.; Jung, C. U.; Park, B. H.; Park, J.-Y.; Cho, Y.; Kim, D.-W.; Jo, J.; Kwon, D.-H.; Kim, M.; Hwang, C. S.; Chae, S. C. Epitaxial Brownmillerite Oxide Thin Films for Reliable Switching Memory. *ACS Appl. Mater. Interfaces* **2016**, *8*, 7902−7911.

(59) Zhang, Q.; Hu, G.; Starchenko, V.; Wan, G.; Dufresne, E. M.; Dong, Y.; Liu, H.; Zhou, H.; Jeen, H.; Saritas, K.; Krogel, J. T.; Reboredo, F. A.; Lee, H. N.; Sandy, A. R.; Almazan, I. C.; Ganesh, P.; Fong, D. D. Phase Transition Dynamics in a Complex Oxide Heterostructure. *Phys. Rev. Lett.* **2022**, *129*, No. 235701.

(60) Ohta, H.; Sato, Y.; Kato, T.; Kim, S. W.; Nomura, K.; Ikuhara, Y.; Hosono, H. Field-Induced Water Electrolysis Switches an Oxide Semiconductor from an Insulator to a Metal. *Nat. Commun.* **2010**, *1*, No. 118.

(61) Cullity, B. D.; Graham, C. D. *Introduction to Magnetic Materials*, 2nd ed.; John Wiley & Sons: Hoboken, NJ, 2009.

(62) Leighton, C. Major Growth in Minor Hysteresis Loops. *Physics* **2010**, *3*, 79.

(63) Pike, C. R.; Roberts, A. P.; Verosub, K. L. Characterizing Interactions in Fine Magnetic Particle Systems Using First Order Reversal Curves. *J. Appl. Phys.* **1999**, *85*, 6660−6667.

(64) Harrison, R. J.; Feinberg, J. M.FORCinel: An Improved Algorithm for Calculating First-Order Reversal Curve Distributions Using Locally Weighted Regression Smoothing *Geochem. Geophys. Geosyst.* 2008; Vol. *9* DOI: 10.1029/2008GC001987.

(65) Gilbert, D. A.; Murray, P. D.; de Rojas, J.; Dumas, R. K.; Davies, J. E.; Liu, K. Reconstructing Phase-Resolved Hysteresis Loops from First-Order Reversal Curves. *Sci. Rep.* **2021**, *11*, No. 4018.

(66) Hwang, H. Y.; Iwasa, Y.; Kawasaki, M.; Keimer, B.; Nagaosa, N.; Tokura, Y. Emergent Phenomena at Oxide Interfaces. *Nat. Mater.* **2012**, *11*, 103−113.

(67) Walter, J.; Wang, H.; Luo, B.; Frisbie, C. D.; Leighton, C. Electrostatic *versus* Electrochemical Doping and Control of

Ferromagnetism in Ion-Gel-Gated Ultrathin $La_{0.5}Sr_{0.5}CoO_{3-\delta}$. *ACS Nano* **2016**, *10*, 7799−7810.

(68) Walter, J.; Charlton, T.; Ambaye, H.; Fitzsimmons, M. R.; Orth, P. P.; Fernandes, R. M.; Leighton, C. Giant Electrostatic Modification of Magnetism via Electrolyte-Gate-Induced Cluster Percolation in $La_{1-x}Sr_xCoO_{3-\delta}$. *Phys. Rev. Mater.* **2018**, *2*, No. 111406.

(69) Walter, J.; Bose, S.; Cabero, M.; Yu, G.; Greven, M.; Varela, M.; Leighton, C. Perpendicular Magnetic Anisotropy via Strain-Engineered Oxygen Vacancy Ordering in Epitaxial $La_{1-x}Sr_xCoO_{3-\delta}$. *Phys. Rev. Mater.* **2018**, *2*, No. 111404.

(70) Walter, J.; Bose, S.; Cabero, M.; Varela, M.; Leighton, C. Giant Anisotropic Magnetoresistance in Oxygen-Vacancy-Ordered Epitaxial $La_{0.5}Sr_{0.5}CoO_{3-\delta}$ Films. *Phys. Rev. Mater.* **2020**, *4*, No. 091401.

(71) Wang, Y.; He, Q.; Ming, W.; Du, M.-H.; Lu, N.; Cafolla, C.; Fujioka, J.; Zhang, Q.; Zhang, D.; Shen, S.; Lyu, Y.; N'Diaye, A. T.; Arenholz, E.; Gu, L.; Nan, C.; Tokura, Y.; Okamoto, S.; Yu, P. Robust Ferromagnetism in Highly Strained $SrCoO_3$ Thin Films. *Phys. Rev. X* **2020**, *10*, No. 021030.

(72) Walter, J.; Yu, G.; Yu, B.; Grutter, A.; Kirby, B.; Borchers, J.; Zhang, Z.; Zhou, H.; Birol, T.; Greven, M.; Leighton, C. Ion-Gel-Gating-Induced Oxygen Vacancy Formation in Epitaxial $La_{0.5}Sr_{0.5}CoO_{3-\delta}$ Films from *In Operando* X-Ray and Neutron Scattering. *Phys. Rev. Mater.* **2017**, *1*, No. 071403.

(73) Rui, X.; Klie, R. F. Atomic-Resolution *In-Situ* Cooling Study of Oxygen Vacancy Ordering in $La_{0.5}Sr_{0.5}CoO_{3-\delta}$ Thin Films. *Appl. Phys. Lett.* **2019**, *114*, No. 233101.

(74) Inkinen, S.; Yao, L.; van Dijken, S. Reversible Thermal Strain Control of Oxygen Vacancy Ordering in an Epitaxial $La_{0.5}Sr_{0.5}CoO_{3-\delta}$ Film. *Phys. Rev. Mater.* **2020**, *4*, No. 046002.

(75) Shiogai, J.; Ito, Y.; Mitsuhashi, T.; Nojima, T.; Tsukazaki, A. Electric-Field-Induced Superconductivity in Electrochemically Etched Ultrathin FeSe Films on $SrTiO_3$ and MgO. *Nat. Phys.* **2016**, *12*, 42−46.

(76) Wang, H.; Postiglione, W. M.; Chaturvedi, V.; Runnerstrom, E. L.; Cleri, A.; Nordlander, J.; Maria, J.-P.; Leighton, C. Electrolyte-Gate-Driven Carrier Density Modulation and Metal−Insulator Transition in Semiconducting Epitaxial CdO Films. *APL Mater.* **2022**, *10*, No. 121106.

(77) An, Q.; Xu, Z.; Wang, Z.; Meng, M.; Guan, M.; Meng, S.; Zhu, X.; Guo, H.; Yang, F.; Guo, J. Tuning of the Oxygen Vacancies in $LaCoO_3$ Films at the Atomic Scale. *Appl. Phys. Lett.* **2021**, *118*, No. 081602.

(78) Mitra, C.; Meyer, T.; Lee, H. N.; Reboredo, F. A. Oxygen Diffusion Pathways in Brownmillerite $SrCoO_{2.5}$: Influence of Structure and Chemical Potential. *J. Chem. Phys.* **2014**, *141*, No. 084710.

(79) Goodenough, J. B.; Park, K.-S. The Li-Ion Rechargeable Battery: A Perspective. *J. Am. Chem. Soc.* **2013**, *135*, 1167−1176.

(80) Choi, S. S.; Lim, H. S. Factors That Affect Cycle-Life and Possible Degradation Mechanisms of a Li-Ion Cell Based on $LiCoO_2$. *J. Power Sources* **2002**, *111*, 130−136.

(81) Bonhôte, P.; Dias, A.-P.; Papageorgiou, N.; Kalyanasundaram, K.; Grätzel, M. Hydrophobic, Highly Conductive Ambient-Temperature Molten Salts. *Inorg. Chem.* **1996**, *35*, 1168−1178.

(82) Lethesh, K. C.; Bahaa, A.; Abdullah, M.; Bamgbopa, M. O.; Susantyoko, R. A. Temperature-Dependent Electrochemical Stability Window of Bis(Trifluoromethanesulfonyl)Imide and Bis-(Fluorosulfonyl)Imide Anion Based Ionic Liquids. *Front. Chem.* **2022**, *10*, No. 859304.

(83) Miyasato, T.; Abe, N.; Fujii, T.; Asamitsu, A.; Onoda, S.; Onose, Y.; Nagaosa, N.; Tokura, Y. Crossover Behavior of the Anomalous Hall Effect and Anomalous Nernst Effect in Itinerant Ferromagnets. *Phys. Rev. Lett.* **2007**, *99*, No. 086602.

(84) Aarbogh, H. M.; Wu, J.; Wang, L.; Zheng, H.; Mitchell, J. F.; Leighton, C. Magnetic and Electronic Properties of $La_{1-x}Sr_xCoO_3$ Single Crystals Across the Percolation Metal-Insulator Transition. *Phys. Rev. B* **2006**, *74*, No. 134408.

(85) Torija, M. A.; Sharma, M.; Gazquez, J.; Varela, M.; He, C.; Schmitt, J.; Borchers, J. A.; Laver, M.; El-Khatib, S.; Leighton, C. Chemically Driven Nanoscopic Magnetic Phase Separation at the $SrTiO_3(001)/La_{1-x}Sr_xCoO_3$ Interface. *Adv. Mater.* **2011**, *23*, 2711−2715.

(86) Wu, J.; Leighton, C. Glassy Ferromagnetism and Magnetic Phase Separation in $La_{1-x}Sr_xCoO_3$. *Phys. Rev. B* **2003**, *67*, No. 174408.

(87) Lee, K. H.; Kang, M. S.; Zhang, S.; Gu, Y.; Lodge, T. P.; Frisbie, C. D. Cut and Stick" Rubbery Ion Gels as High Capacitance Gate Dielectrics. *Adv. Mater.* **2012**, *24*, 4457−4462.